Design and trial implementation of a continental-scale, kilometre-resolution hourly precipitation analysis for Australia using satellite, radar and gauges

Yuhang Zhang[1], Quan J. Wang[4, 1], Andrew J. Frost[2], Jayaram Pudashine[3], Blair Trewin[3], Carlos Velasco-Forero[3], Chun-Hsu Su[3], Vincent Villani[3]

[1]Department of Infrastructure Engineering, The University of Melbourne, Parkville, VIC 3010, Australia
[2]Bureau of Meteorology, Sydney, NSW 1300, Australia
[3]Bureau of Meteorology, Melbourne, VIC 3001, Australia
[4]College of Hydrology and Water Resources, Hohai University, Nanjing 210098, China

Correspondence to: Quan J. Wang (quan.wang@unimelb.edu.au) and Andrew J. Frost (andrew.frost@bom.gov.au)

Abstract. High-resolution precipitation information is essential for hydrometeorological applications such as extreme weather monitoring, flood forecasting, and disaster risk management. Despite substantial advances in satellite, radar, and gauge observations, producing kilometre-resolution sub-daily precipitation analyses over continental domains remains challenging due to heterogeneous data availability, scale mismatches, and computational constraints. This study presents the design and trial implementation of BRAIN (blended rainfall), a continental-scale, kilometre-resolution hourly precipitation analysis for Australia. In this initial implementation, BRAIN integrates three key data sources from the Australian Bureau of Meteorology: geostationary satellite rainfall estimates (2 km, 10 min) from Himawari, radar rainfall estimates (1 km, 5 min) from the national radar network, and rainfall observations from sub-daily rain gauges. The trialled system incorporates quality control, spatiotemporal aggregation, bias correction, and a simplified statistical interpolation configuration designed to balance analysis performance and computational scalability at the continental scale. Source contributions are weighted according to their spatial and temporal error characteristics, allowing each data type to influence the analysis where it is most informative. The initial implementation produces hourly rainfall fields at 2-km resolution across the Australian continent. Evaluation over the 2022–2023 trial period indicates that the blended analysis improves overall upon satellite-only, radar-only, and satellite–gauge products. Comparisons with gauge-based interpolation and the current daily operational product further illustrate the spatial characteristics of the blended analysis, including finer-scale rainfall structures and intensity variations that are not represented by these products. These results demonstrate the feasibility of the proposed design for continental-scale, high-resolution multi-source precipitation analysis in the Australian context, with potential applications to long-term historical reconstruction and near-real-time rainfall analysis. The flexible and scalable system design also allows future upgrades, including finer spatial and temporal resolutions and the incorporation of additional data sources. Beyond

Australia, this study provides a practical reference for developing large-scale multi-source precipitation analyses at kilometre and hourly resolutions.

1 Introduction

Precipitation is a critical component of the water cycle, exerting strong control over hydrological processes and acting as a primary driver of flooding, which poses significant risks to infrastructure and human safety (Prein et al., 2017). However, accurately characterising precipitation fields, particularly at high spatial and temporal resolutions, remains challenging due to their pronounced variability across scales (Nishant et al., 2022; Zhang et al., 2021a).

Multiple observational sources provide complementary information for characterising precipitation. Rain gauges provide relatively direct and reliable measurements at individual locations but have limited ability to represent spatial variability, particularly in regions with sparse observation networks (Villarini et al., 2008). Weather radars provide precipitation estimates at high spatial and temporal resolutions over broader areas but are typically concentrated in densely populated regions, leaving large remote areas unmonitored (e.g., Zhang et al., 2025). Satellite-based precipitation products provide extensive spatial coverage and frequent temporal sampling, offering valuable precipitation information where ground-based observations are unavailable (e.g., Sun et al., 2018; Zhang et al., 2021b, c). Reanalysis products combine numerical weather prediction models with assimilated observations to provide spatially and temporally complete precipitation fields, although their precipitation estimates depend on model configuration, physical parameterisations, spatial resolution, and data assimilation systems (e.g., Su et al., 2019, 2021, 2025).

Despite these complementary strengths, each source is subject to distinct uncertainties. Gauge measurements can be affected by instrumental errors (e.g., wind-induced undercatch) and local sampling limitations (e.g., discrete tipping in tipping-bucket gauges) (Ciach, 2003; Dunn et al., 2025; Ochoa-Rodriguez et al., 2019; Segovia-Cardozo et al., 2023), while their point-scale measurements may not fully represent precipitation averaged over a larger grid cell. Radar precipitation estimates are affected by uncertainties associated with reflectivity-to-rainfall conversion (Kirsch et al., 2019), attenuation (Delrieu et al., 1999), beam blockage (McRoberts and Nielsen-Gammon, 2017), ground clutter (Hubbert et al., 2009a, b), and range-dependent sampling (Ochoa-Rodriguez et al., 2019). Satellite precipitation estimates rely on indirect relationships between remotely sensed cloud or hydrometeor properties and surface precipitation and are therefore subject to retrieval and algorithmic uncertainties, including difficulties in detecting or quantifying certain precipitation regimes (Chen et al., 2023; Li et al., 2026; So and Shin, 2018; Upadhyaya et al., 2020; Zhu et al., 2026). Reanalysis precipitation is also subject to uncertainties inherent in its production process, as precipitation is generally diagnosed by the numerical model rather than directly assimilated, with its accuracy therefore depending strongly on model physics and parameterisations (e.g., Su et al., 2019, 2021, 2025). These errors can vary substantially across space, time, and precipitation conditions. Integrating

information from multiple sources therefore provides an opportunity to leverage their complementary strengths while reducing dependence on the limitations of any individual source (e.g., Beck et al., 2017, 2019).

A range of approaches have been developed for multi-source precipitation blending (e.g., Xu et al., 2024; Zhang et al., 2025). For example, performance-based averaging methods derive weights for non-gauge data sources from gauge-based skill metrics and apply them in a grid-aligned manner, but their applicability may be limited in regions with very sparse gauge coverage. Triple collocation-based approaches provide a gauge-independent alternative by estimating weights from independent data sources (e.g., Dong et al., 2022; Koster et al., 2021; Xu et al., 2020). However, both performance-based and triple collocation-based approaches typically require spatially complete datasets and assign fixed source weights over time, limiting their applicability under heterogeneous data coverage, such as mixtures of spatially incomplete gridded fields and point observations. Multifractal blending methods aim to combine precipitation information across spatial scales (e.g., Imhoff et al., 2023; Renzullo et al., 2017), but their implementation can be challenging when consistent scaling behaviour is not evident in the input data. Physically based approaches have also been developed, in which dynamic weighting rules are assigned according to observational quality and environmental conditions, including those used in the operational national-scale Multi-Radar Multi-Sensor (MRMS) system in the United States (e.g., Martinaitis et al., 2020).

More recently, machine learning-based approaches have been explored (e.g., Gavahi et al., 2023; Kossieris et al., 2024; Xu et al., 2024), in which non-gauge data sources are treated as input features and model relationships are learned using gauge observations as targets. While offering high flexibility, ML-based approaches have limited interpretability and substantial computational demands, which have constrained their adoption in operational precipitation analysis. In addition, many of the above approaches typically do not assimilate gauge observations directly as a primary data source in the blending step, which can limit performance in gauge-rich regions where point observations provide the most accurate precipitation information.

Compared with the approaches discussed above, statistical interpolation, also known as optimal interpolation, is a statistical method with several properties that are well suited to multi-source precipitation blending (e.g., Bhargava and Danard, 1994; Chua et al., 2022a, 2023; Fortin et al., 2018; Gandin, 1965; Mahfouf et al., 2007; Shen et al., 2014, 2018). A defining feature of statistical interpolation is that rain gauge observations are explicitly assimilated as a primary data source, rather than being used only indirectly for weight estimation, bias correction, or model training. The grid-wise, time-step-wise formulation combines a spatially complete background field with observational increments weighted according to error characteristics and spatial proximity. This structure enables the flexible integration of point and gridded observations while accommodating spatial and temporal data gaps, making statistical interpolation well suited to large-scale precipitation analysis under conditions with heterogeneous data availability.

Building on these properties, multi-source precipitation analysis or reanalysis systems have been developed and implemented in several countries, including the United States (e.g., Xie et al., 2010), Canada (e.g., Fortin et al., 2015, 2018;

Khedhaouiria et al., 2020, 2022; Mahfouf et al., 2007), the United Kingdom (e.g., Yu et al., 2020), China (Shen et al., 2014, 2018; Xia and Wang, 2025; Xie and Xiong, 2011), and France (e.g., Hyfte et al., 2023), with a wide range of spatial and temporal resolutions. In practice, the achievable spatial and temporal resolution of such systems is largely constrained by the data source used for the background field. For example, systems based on global satellite products and NWP outputs commonly operate at spatial resolutions of around 10 km unless additional interpolation or downscaling is applied, with temporal resolutions typically ranging from hourly to several-hourly intervals, depending on data availability and computational cost. Although these systems generally follow similar blending principles, each implementation must be tailored to regional data availability, blending configuration, computational capacity, and operational requirements, and must be maintained through routine updates as observing systems evolve.

In Australia, several gridded precipitation products based on daily gauge observations have been developed to support climate and water-related applications (e.g., Jeffrey et al., 2001; Jones et al., 2009; Evans et al., 2020). For example, the Australian Gridded Climate Data (AGCD) product, formerly known as the Australian Water Availability Project (AWAP) product (Jones et al., 2009), provides an operational 5-km daily rainfall dataset that is widely used, with a higher-resolution version (i.e., 1 km) recently developed by the Australian Bureau of Meteorology (hereafter, the Bureau) (Bari et al., 2026). Despite these advances, there is currently no national operational gridded rainfall product that provides high-resolution precipitation at sub-daily timescales (e.g., hourly). This gap is particularly relevant to flood modelling and forecasting, which require rainfall information at sub-daily timescales. In the Bureau's operational flood forecasting system, inverse distance weighting (IDW) interpolation is used to derive catchment- and/or sub-catchment-scale rainfall estimates from sub-daily gauge observations for hydrological modelling (Malone, 1999; Malone and Carroll, 2022), rather than to generate a national gridded rainfall product. While radar-based rainfall products (Seed et al., 2007) offer high spatial and temporal resolution, their limited coverage leaves a substantial fraction of the Australian land area unmonitored (approximately 28% in 2023), particularly in remote regions (see Fig. 1c). Satellite-derived sub-daily precipitation estimates are also available, but their relatively coarse resolution (e.g., 10 km) and uncertainty constrain their suitability compared with gauge-based analyses (Islam et al., 2020).

The lack of a national, high-resolution sub-daily rainfall product highlights the need for a multi-source precipitation analysis for Australia (Nishant et al., 2022). Several experimental efforts have sought to address this gap. Disaggregation approaches infer sub-daily rainfall from daily products using high-frequency data such as reanalysis (Acharya et al., 2022), but their accuracy depends on the ability of reanalysis to realistically represent sub-daily precipitation and is further limited by data latency for near-real-time applications (e.g., Su et al., 2025). Blending-based studies have demonstrated the potential of integrating multiple data sources, including satellite–gauge merging using statistical interpolation at the monthly scale (Chua et al., 2022a, b) and catchment-scale blending of NWP, satellite, and radar data using multifractal methods (Renzullo et al., 2017). However, these efforts have not yet resulted in a national-scale, kilometre-resolution, sub-daily rainfall product.

Recently, the Bureau has implemented the Himawari-based Convective Rainfall Rate from Cloud Physical Properties (CRRPH) product, which offers markedly higher spatial (2 km) and temporal (10 min) resolutions than existing global satellite products such as the Integrated Multi-satellite Retrievals for Global Precipitation Measurement (IMERG, 10 km and 30 min), with frequent updates (15 min) suitable for near-real-time applications (Bureau of Meteorology, 2024). These characteristics provide a promising basis for developing kilometre-resolution, sub-daily precipitation analyses at the national scale.

As part of recent national efforts to advance high-resolution precipitation analysis, the Bureau has initiated the *Next Generation Rainfall Project*. The project aims to develop a new generation of rainfall products to support both historical applications, such as climate analysis and hydrological model calibration, and near-real-time operational applications, including flood forecasting and disaster response. Within this context, this paper presents the design and national-scale trial implementation of BRAIN (Blended Rainfall). BRAIN is a multi-source precipitation analysis system that produces hourly rainfall fields at 2-km resolution across Australia by integrating satellite, radar, and sub-daily gauge observations within a statistical interpolation framework.

The study makes several key contributions:

(i) It systematically examines the role of the latest Himawari CRRPH satellite rainfall product as a high-resolution background field and investigates its interaction with radar and sub-daily gauge observations within the blended analysis, building on recent advances by the Bureau in satellite-based rainfall estimation.

(ii) It presents a continental-scale trial implementation for Australia that integrates all currently available and operationally manageable satellite, radar, and gauge observations within a unified framework, extending previous multi-source efforts towards a potentially national operational product.

(iii) It applies and adapts statistical interpolation theory to Australian observational and computational constraints, including the adoption of an error-informed localisation strategy and a simplified nearest-point representation for radar observations. These adaptations enable scalable, grid-cell-wise and time-step-wise blending at kilometre and hourly resolutions with low computational overhead.

The resulting blended analysis is evaluated from multiple complementary perspectives, including comparisons with single-source fields, two-source blending configurations, and existing operational products and approaches. The BRAIN framework is designed to be extensible, scalable, and transferable. It allows for the future incorporation of additional data sources, including alternative satellite products, numerical weather prediction (NWP) outputs or reanalysis products, and daily gauge observations (e.g., Zhang et al., 2027). The framework also supports adaptation to finer spatial or temporal resolutions (e.g., 1 km and 30 min) as operational and research needs evolve and as computational resources increase. Beyond the Australian context, BRAIN provides a practical reference for large-scale multi-source precipitation analysis at kilometre and hourly

resolutions, complementing existing regional-, national-, and basin-scale implementations under heterogeneous observational conditions.

2 Data sources

Many different data sources are possible for use in generating a blended precipitation product for Australia. In the first instance, we use three Bureau-managed precipitation data sources for blending:

- In situ rain gauges (15/30-min data aggregated to hourly) from the Bureau and those supplied operationally by other jurisdictional agencies to support the Bureau's flood forecasting and warning responsibilities.
- Radar rainfall rates (5-min, 1-km grid) from the Bureau's national radar network.
- Satellite rainfall estimates processed from Himawari (10-min, 2-km grid).

As detailed further below, these data feeds were chosen for the initial implementation for two main reasons: (1) all three data sources (in situ gauges, radar, and satellite) are currently operational, ensuring both feasibility and immediate applicability; and (2) among these, in situ gauge observations are already used operationally to support national flood forecasting services and provide the primary observational reference for evaluation in this study. Additional datasets are being considered for future upgrades (see Section 5.3 for future directions). The 2022–2023 period was used for trial development and evaluation to assess the performance of the initial implementation under near-current observational conditions.

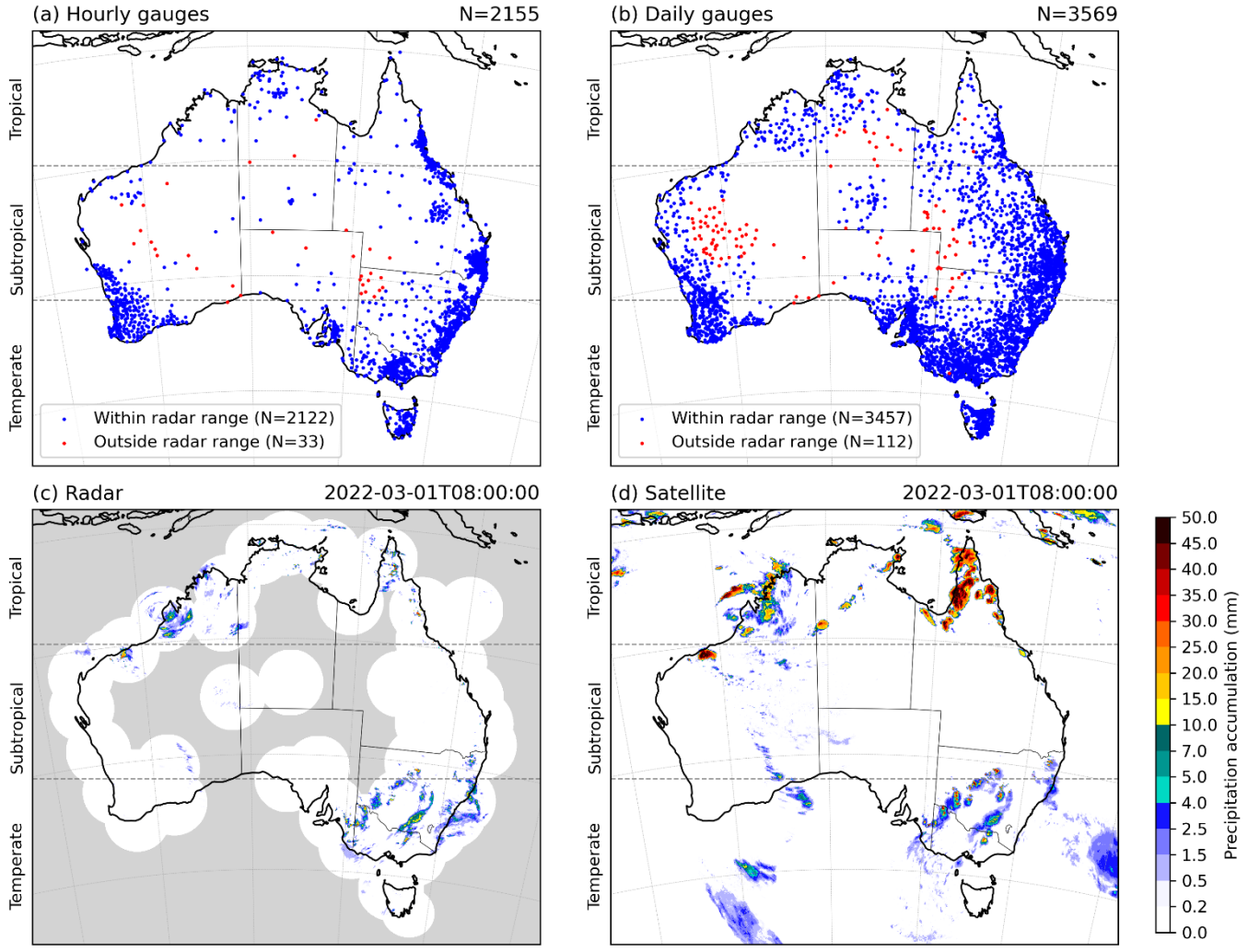


Figure 1. Spatial distribution and coverage of the data sources used in this study: (a) hourly gauges (aggregated from sub-daily observations; N = 2,155) categorised as within (N = 2,122, blue) or outside (N = 33, red) the maximum radar range, (b) daily gauges (N = 3,569) similarly categorised as within (N = 3,457, blue) or outside (N = 112, red) the maximum radar range, (c) radar-based hourly precipitation accumulation at 08:00 UTC on 1 March 2022, with a maximum radar range of approximately 300 km and a spatial resolution of 1 km, and (d) satellite-based precipitation (CRRPH) for the same time, with seamless spatial coverage at a 2-km resolution. The tropical, subtropical, and temperate subregions used in subsequent analyses are indicated by the horizontal dashed lines.

2.1 In situ observations

A total of 2,155 sub-daily rain gauge stations (with observations aggregated to hourly resolution; Fig. 1a) and 3,569 independent daily rain gauge stations (Fig. 1b) (Bureau of Meteorology, 2025) were used in this study. The hourly gauges,

sourced from both automatic weather stations and flood warning stations, were recorded at sub-hourly intervals and served as the primary input for the blending process. The daily gauges, obtained primarily from human-recorded observations, provided an independent evaluation dataset for the final blended product. To prevent redundancy, any gauge present in both datasets was retained only in the hourly dataset. The network density varies significantly for hourly gauges (Fig. 1a), with some areas—particularly along the populated and flood-prone Great Dividing Range in eastern Australia—having dense coverage, while others have little to no data. In contrast, daily gauges (Fig. 1b) are more evenly distributed, though substantial data voids remain, particularly in the arid and sparsely populated western interior.

Both the hourly and daily datasets were subjected to rigorous quality control procedures, including checks for anomalously high values based on historical rainfall distributions and gridded Intensity-Frequency-Duration (IFD) statistics. Additional procedures included spatial intercomparisons to detect anomalously high values or prolonged periods of zero values indicative of instrument failure or gauge blockage, intercomparisons between sub-daily and daily observations where both were available, and checks for long sequences of identical non-zero values. Specifically, potential rainfall spikes were identified using thresholds of two and four times the historical 99.9th percentile. Extreme rainfall observations were also checked against local IFD statistics, including the 1% Annual Exceedance Probability (AEP) and 1-in-1000-year rainfall thresholds. Spatial consistency checks further compared unusually high observations with neighbouring gauges within 50 km. These complementary checks used historical, climatological, and spatial information to identify potentially erroneous high rainfall values while retaining plausible extreme rainfall observations.

Although the quality control procedures remove many identifiable erroneous observations, residual measurement and sampling uncertainties may remain in the gauge data used in this study. The hourly observations are aggregated from sub-hourly measurements, primarily from tipping-bucket gauges, and may therefore retain uncertainties associated with the original sub-hourly measurements and their aggregation into hourly totals. In addition, some isolated gauges have few nearby reference stations available for spatial consistency checks, while random or less readily identifiable errors may not be detected by the quality control procedures. It is also worth noting that rainfall measured by an individual gauge may differ from the corresponding 2-km grid-cell average because of sub-grid precipitation variability, introducing spatial representativeness uncertainty when point observations are used to represent gridded precipitation.

An additional independent hourly dataset (approximately 2,000 stations) was obtained from third-party providers, including local councils, water utilities, and other water management organisations through ongoing data-sharing arrangements. As this dataset continued to expand throughout the project, these observations became available only after completion of the bias correction and blending analyses and were therefore used for supplementary independent validation. These observations were subjected to the same quality control procedures as the primary hourly gauge dataset. The spatial distribution of these hourly gauge stations is shown in Fig. S15.

2.2 Radar-based observations

Radar rainfall estimates (Bureau of Meteorology, 2022) were obtained from the Bureau's operational Rainfields system, which provides real-time data at a spatial resolution of 1 km and a temporal resolution of 5 min. Weather radar observations have been available in Australia since the late 1990s, with the network progressively expanding from coverage concentrated around major population centres to its current broader coverage. The radar network during 2022–2023 used in this study covered approximately 72% of the Australian land area. Further information on Australian weather radar data availability and archiving is provided by the Australian Unified Radar Archive (https://opus.nci.org.au/spaces/NDP/pages/399803502/Australian+Unified+Radar+Archive).

The Rainfields system offers both raw and calibrated radar rainfall rates. Raw rainfall rates are derived using reflectivity–rainfall rate (Z–R) relationships, which are established for each radar based on long-term historical data. Calibrated rainfall rates are then generated by applying dynamic bias correction to the raw estimates using nearby gauge observations within a 150-km radius and a 15-min time window, employing a Kalman filtering approach (Chumchean et al., 2006). By incorporating real-time gauge data, calibrated radar rainfall rates provide an additional refinement to the Z-R-based estimates, allowing adjustments to reflect current conditions that may deviate from those during the historical period used to derive the Z-R relationships.

In this study, we used hourly radar accumulations derived from 5-min calibrated radar rainfall rates as a blending input at the target hourly resolution. However, we recalibrated the radar data using gauges within a 300-km radius and a 1-hour window to increase the availability of co-located radar-gauge pairs for estimating local radar errors. The larger spatial radius allows more co-located radar-gauge pairs to be included, particularly in gauge-sparse regions, while the longer temporal window increases gauge availability by accommodating their reporting latency. These two modifications therefore address the spatial and temporal availability of gauge information, respectively. We refer to the operational calibrated product as R0 and the recalibrated version as R1. In addition, to match the spatial resolution of the satellite data, the original 1-km radar grids were aggregated to 2 km. Figure 1c shows an example of the recalibrated hourly radar rainfall accumulation (R1) across Australia at 08:00 UTC on 1 March 2022.

The R1 radar estimates used for blending benefit from both the operational Rainfields calibration and the additional hourly gauge-based recalibration applied in this study. Nevertheless, residual errors and artefacts present in the underlying radar observations may remain after these corrections. For example, local effects associated with beam blockage, anomalous echoes, and other retrieval or sampling issues may not always be fully identified or removed during operational quality control and processing.

In addition, the gauge-based bias correction estimates local radar biases from available gauge observations and interpolates these estimates to construct spatially continuous bias fields. However, this correction does not necessarily remove biases across all precipitation intensities, and residual biases may remain within specific rainfall intensity ranges. Its effectiveness

also depends on the availability and representativeness of nearby gauges and on how well the interpolated bias field represents the spatial variability of the actual radar bias. The correction may therefore be less effective in areas far from available gauges or with sparse gauge coverage. Details of the bias-correction procedure are provided in Section 3.3.

2.3 Satellite-based observations

The Himawari-based CRRPH v2.1 product (Bureau of Meteorology, 2024) was selected as the background field for this study because it provides continental coverage at a spatial resolution of 2 km and a temporal resolution of 10 min, helping to compensate for gaps in the ground-based observation network. The product is derived from observations collected by the Japanese Himawari-8/9 geostationary satellites, which carry the Advanced Himawari Imager (AHI) and provide multi-spectral observations of cloud and atmospheric properties over the Australian region. CRRPH exploits the high-frequency, multi-channel infrared observations from AHI to infer convective rainfall rates based on cloud physical properties, including cloud optical depth and effective radius.

The CRRPH product is available from 2015 onwards and is updated operationally with a latency of approximately 15 minutes, making it suitable for near-real-time applications. In this study, the native 2-km spatial resolution of CRRPH was adopted as the target grid for blending, thereby defining a common spatial grid across all input datasets. This choice avoids additional spatial resampling of the satellite field and reduces potential interpolation-induced errors. Temporally, the 10-min CRRPH rainfall rates were aggregated to hourly accumulations prior to blending to ensure consistency with other data sources and downstream hydrological applications. Figure 1d illustrates an example of the CRRPH hourly rainfall accumulation across Australia at 08:00 UTC on 1 March 2022, highlighting its ability to represent large-scale precipitation patterns with fine spatial detail. As with other satellite-based precipitation products, CRRPH rainfall estimates are subject to systematic biases.

As an infrared satellite precipitation product, CRRPH infers surface rainfall indirectly from cloud properties observed by the Himawari AHI. Retrieval errors may therefore occur when the observed cloud characteristics do not adequately represent the occurrence or intensity of surface precipitation (Karagiannidis et al., 2023; So and Shin, 2018). In addition, the calibrated lookup tables used to convert retrieved cloud properties into rainfall rates represent empirical relationships and may not fully capture variations in the cloud–rainfall relationship under different precipitation conditions.

To reduce systematic discrepancies with gauge observations, a spatially varying local bias correction was applied, as described in Section 3.3. S0 denotes the original CRRPH product without bias correction, while S1 denotes the bias-corrected product used as the background field for blending. The correction is designed to reduce the overall systematic bias of CRRPH relative to gauge observations towards zero, but does not necessarily remove biases across all precipitation intensities. Residual biases may therefore remain within specific rainfall intensity ranges. Moreover, the correction cannot fully address errors in rainfall occurrence or spatial structure inherent in the satellite retrieval. As the estimated bias field is

derived from available gauges and spatially interpolated, its effectiveness depends on the availability and representativeness of nearby gauges and may be reduced in areas far from available gauges or with sparse gauge coverage.

3 Methods

3.1 Workflow

The multi-source blending workflow (Fig. 2) integrates satellite, radar, and gauge data through a multi-step process to produce a high-resolution blended rainfall product. After temporal and spatial aggregation, quality control, and bias correction, satellite data serve as the background field, radar data as the first-layer observations, and gauge data as the second-layer observations. These inputs are then combined using the multi-source statistical interpolation framework to generate the final blended rainfall (BRAIN) product. The key processing steps are described in the following subsections.

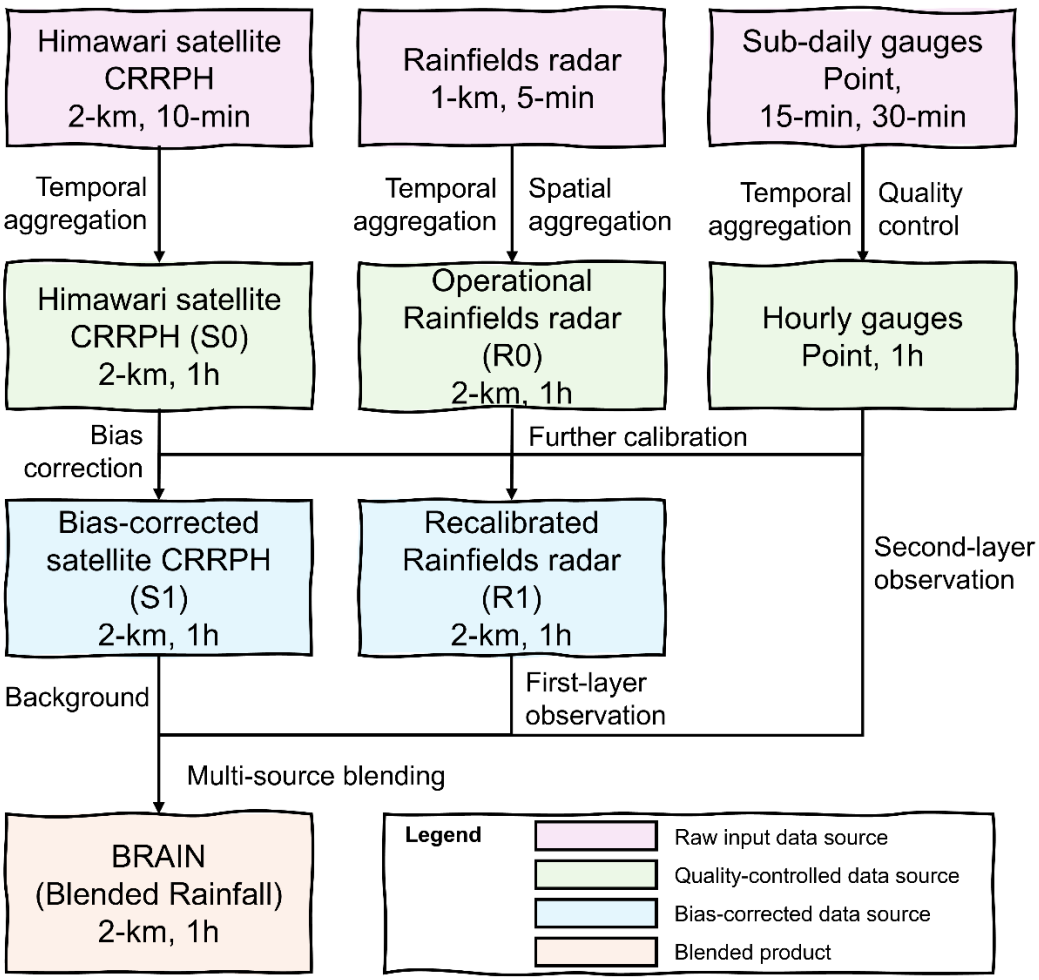


Figure 2. Workflow of the multi-source statistical interpolation blending process used in the BRAIN (Blended Rainfall) analysis. The inputs include Himawari satellite CRRPH data (2 km, 10 min), Rainfields radar data (1 km, 5 min), and sub-daily gauge observations (point data, 15/30 min). The workflow includes temporal aggregation of satellite, radar and gauge data, spatial aggregation of radar data, and quality control of gauge observations. After bias correction, the satellite data serves as the background field, radar data serve as the first-layer observations, and gauge data serve as the second-layer observations. The trialled implementation integrates these inputs to generate the final BRAIN analysis at a spatial resolution of 2 km and a temporal resolution of 1 hour.

3.2 Multi-source statistical interpolation

A range of approaches have been developed for producing blended gridded datasets (e.g., Yin et al., 2021; Gavahi et al., 2023; Khedhaouiria et al., 2022; Chappell et al., 2013; Shen et al., 2014; Yu et al., 2020; Zhang et al., 2025). Statistical interpolation, also commonly referred to as optimal interpolation (OI), was originally developed within the framework of objective meteorological analysis (Gandin, 1965) and has been widely used as an interpolation method by many meteorological organisations (e.g., Mitchell et al., 1990; Huang et al., 1997; De Mey, 1994; Lorenc et al., 1991) for blending or assimilating observations with weather models, particularly before the development of more advanced variational methods (e.g., Gauthier et al., 2007; Rawlins et al., 2007; Rabier et al., 2000; Rabier, 2005). More recently, OI and related statistical interpolation approaches have been widely applied to precipitation interpolation and blending (e.g., Bergman, 1978; Chua et al., 2022c; Mahfouf et al., 2007; Xia and Wang, 2025; Xie and Xiong, 2011; Yu et al., 2020).

Statistical interpolation enables the integration of multi-source precipitation data by updating a *background* estimate—in this case, the satellite-derived first guess—based on *observations* (gauge and radar data) to generate an *analysis*, with adjustments weighted according to the estimated error characteristics of each data source. The formulation adopted in this study follows the established OI framework (Gandin, 1965; Xie and Xiong, 2011; Yu et al., 2020; Mahfouf et al., 2007; Zhang et al., 2026), as described by Eqs. (1)–(5) below. A detailed derivation of the formulation is provided in our recent study (Zhang et al., 2026). The method assumes Gaussian error distributions, which may not strictly hold for precipitation but are commonly used as an approximation to avoid the additional complexity associated with data transformation, while bias correction is applied to both satellite and radar data to help satisfy the assumption of unbiased errors. Statistical interpolation operates as an iterative, grid-based analysis, adjusting each target grid cell using observations within a predefined search radius (e.g., 200 km in this study).

For a given target grid cell k, the analysis value is computed as:

$$A_k = B_k + \sum_{i=1}^{n} w_i \cdot (O_i - B_i) \quad (1)$$

where A_k is the analysis value, B_k is the background value, O_i is the observation value at a nearby location i, and B_i is the corresponding background value, n is the total number of nearby observations. The term $O_i - B_i$ represents the observation increment, and w_i are the weights assigned to each observation.

The analysis error at the target gird cell k, denoted by E_k, is then determined as the difference between the theoretical "true value" T_k and the analysis value A_k:

$$E_k^2 = (T_k - A_k)^2 = [T_k - B_k - \sum_{i=1}^{n} w_i \cdot (O_i - B_i)]^2 \quad (2)$$

Here, T_k denotes the unknown theoretical true value at the target grid cell k, which cannot be directly observed in practice and is introduced for error definition and derivation purposes.

By defining the background error $f_i = T_i - B_i$ and observation error $\varepsilon_i = O_i - T_i$, the analysis error equation can be rewritten as:

$$E_k^2 = [f_k - \sum_{i=0}^{n} w_i \cdot (f_i + \varepsilon_i)]^2 \quad (3)$$

Minimising this error allows us to optimally assign weights to nearby observations, yielding the most statistically accurate estimate for each target grid cell. To solve this optimization problem, we take the partial derivative of E_k^2 with respect to each w_i and set it to zero, which leads to the following equation:

$$\sum_{j=1}^{n}(f_i + \varepsilon_i)\left(f_j + \varepsilon_j\right)w_i = f_k(f_i + \varepsilon_i),\ i = 1,2,\dots,n \quad (4)$$

By expanding and expressing Eq. 4 in standardised form:

$$\sum_{j=1}^{n}\left(\mu_{ij} + \tau_{ij}\sigma_j + \tau_{ji}\sigma_i + \rho_{ij}\sigma_i\sigma_j\right)w_i' = \mu_{ki} + \tau_{ki}\sigma_i,\ i = 1,2,\dots,n \quad (5)$$

where:

- $\mu_{ij} = f_i f_j / \left({f_i}^2 {f_j}^2\right)^{\frac{1}{2}}$, $\mu_{ij} \in \mathbb{R}^{n\times n}$ is the background (satellite) error correlation between the *i*th and *j*th observation locations. Similarly, $\mu_{ki} \in \mathbb{R}^{1\times n}$ is the background error correlation between the target grid cell *k* and the *i*th observation location.
- $\tau_{ij} = f_i \varepsilon_j / \left({f_i}^2 {\varepsilon_j}^2\right)^{\frac{1}{2}}, \tau_{ij} \in \mathbb{R}^{n\times n}$ is the correlation between the background error at the *i*th location and the observation error at the *j*th location. Similarly, τ_{ki} is the correlation between the background error at the target grid cell *k* and the observation error at the *i*th observation location.
- $\rho_{ij} = \varepsilon_i \varepsilon_j / \left({\varepsilon_i}^2 {\varepsilon_j}^2\right)^{\frac{1}{2}}, \rho_{ij} \in \mathbb{R}^{n\times n}$ is the observation error correlation between the *i*th and *j*th observation locations.
- $\sigma_i = \left({\varepsilon_i}^2 / {f_i}^2\right)^{\frac{1}{2}}, \sigma_i \in \mathbb{R}^{n\times 1}$ is the ratio of the standard deviation of the observation error to the standard deviation of the background error at the *i*th observation location.

- $w_i' = w_i\left(f_i^{\,2}/f_k^{\,2}\right)^{\frac{1}{2}}, w_i' \in \mathbb{R}^{n\times 1}$ is the scaled weight accounting for differences in background error between the *i*th observation location and the target grid cell *k*.

This system of linear equations is solved to determine the optimal weights w_i, which are used to obtain the optimal precipitation estimate at each target grid cell by combining information from the background field and available observations (e.g., radar and gauge data). The treatment of different observation sources is described below, while the corresponding source-specific error characteristics are introduced in Section 3.4.

These equations require knowledge of the background error correlations (μ_{ij}, μ_{ki}), background-to-observation error correlations (τ_{ij}, τ_{ki}), observation error correlations (ρ_{ij}), the ratios of observation to background error variances (σ_i), and the spatial variation in background errors ($f_i^{\,2}/f_k^{\,2}$).

The background error correlation is typically derived from an analytical function (e.g., Bergman, 1978; Xie and Xiong, 2011; Yu et al., 2020), while background-to-observation error correlations are assumed to be zero, as errors from different sensor systems are considered independent. Similarly, the observation-to-background error variance ratio is estimated separately for satellite, radar, and gauge data using analytical functions (e.g., Bergman, 1978; Xie and Xiong, 2011; Yu et al., 2020), with the corresponding ratios computed between different data sources. The most challenging part of statistical interpolation is determining the observation error correlations (ρ_{ij}), as this requires accounting for the number of observations in different cases and their respective sensor systems, particularly as the number of data sources increases.

In this study, both gauge and radar data are incorporated as observations. Radar–gauge observation error cross-correlations are assumed to be zero. Explicit estimation of these cross-correlations requires independent characterisation of both radar and gauge errors. In particular, robust estimation of gauge representativeness errors generally requires a sufficiently dense gauge network to provide an independent estimate of areal rainfall, which is difficult to achieve consistently across Australia. Seo et al. (2011), using high-density gauge networks, showed that radar–gauge error correlations can vary across individual samples and scales, but their mean correlations remained close to zero across the spatial and temporal scales examined. We therefore adopt zero radar–gauge error cross-correlation as a practical simplifying assumption for the national-scale implementation. Furthermore, errors from gauges at different locations are also assumed to be independent. Accordingly, radar–gauge and gauge–gauge observation error correlations are set to zero. However, a full representation of radar-to-radar error correlations would require retaining potentially hundreds of radar grid cells within the influence radius (e.g., 200 km in this study) for each target grid cell, substantially increasing the size of the observation-error covariance matrix (i.e., in Eq. (5)), computational cost, and risk of matrix rank deficiency.

To address this issue, an error-informed localisation strategy is adopted within the statistical interpolation framework. Specifically, a highly efficient implementation is introduced in which only the nearest radar grid cell within a 200 km search radius, identified as the grid cell with the minimum Euclidean distance to the target grid cell, is retained as a supplementary

observation. If no valid radar grid cell is available within this radius, no radar observation is included for that target grid cell. The 200 km radius defines the maximum search range, while the effective influence of the selected radar observation is further controlled by the distance-dependent error correlation function. In cases where multiple grid cells have the same minimum distance, the grid cell with the lowest error variance is retained. This nearest-point approximation reflects a deliberate selection strategy that prioritises the most locally relevant radar information while avoiding dilution by redundant contributions. Consequently, each local analysis contains at most one radar observation, and no radar–radar error covariance terms arise in the resulting observation-error covariance matrix. The suitability of this nearest-point approximation has been evaluated in our previous study (Zhang et al., 2026). As a result, this approach enables scalable, grid-cell-wise blending suitable for continental-scale precipitation analysis at kilometre-scale spatial and hourly temporal resolutions under practical computational constraints.

The design offers several advantages. First, it substantially reduces computational complexity by limiting the number of radar observations included in the statistical interpolation linear system, which is particularly important for continental-scale applications in Australia involving more than five million grid cells. Second, because each local analysis contains at most one radar observation, it avoids the need to explicitly represent radar-to-radar error correlations, thereby simplifying the modelling chain and reducing the number of processing steps. Third, by constraining the spatial influence of radar observations, the approach limits error extrapolation, an important consideration given the directional and range-dependent nature of radar errors. Finally, despite its simplicity, the strategy allows radar observations to contribute effectively both within and outside radar coverage, ensuring consistency and spatial continuity across data sources in the blended rainfall fields.

Following the above strategy and design, we solve the simplified system of linear equations given by Eq. (5):

$$\sum_{j=1}^{n}\left(\mu_{ij} + \rho_{ij}\sigma_i\sigma_j\right) w_i' = \mu_{ki},\ i = 1,2,\dots,n \quad (6)$$

where n represents the number of available observations within the search radius, which is set to 200 km in the trial implementation. A sensitivity test using an alternative search radius of 100 km showed only minor differences compared with the 200-km configuration (Fig. S23). We therefore retained the 200-km radius as a conservative choice to avoid excluding potentially useful observations, although this incurs a slightly higher computational cost than using a 100-km radius.

The number of observations varies depending on data availability and includes five possible cases: (1) a single radar grid cell, (2) a single gauge, (3) multiple gauges, (4) one or more gauges combined with one radar grid cell, and (5) no available gauge or radar observations. For cases involving multiple gauges, up to the 20 nearest gauges within the 200-km search radius are used. When a radar observation is also present, the total number of observations does not exceed 21. This system size remains computationally manageable.

In Eq. (5), the background-to-observation error correlation terms, including τ_{ij}, τ_{ji} and τ_{ki}, are assumed to be zero. This assumption reflects the negligible correlations between background and observation errors and leads directly to the simplified formulation in Eq. (6). And then gauge-to-gauge error correlations are assumed to be zero between different locations and equal to one at the same location. Under the nearest-point approximation, only a single radar observation is included. Gauge–radar error correlations are also assumed to be negligible. Under these assumptions, the observation error correlation matrix $\boldsymbol{\rho}$ reduces to the identity matrix ($\boldsymbol{\rho}= \mathbf{I}$). The radar observation contributes only through its self-correlation, which is represented by the final diagonal element and set to one.

With these simplifications, the linear system remains computationally efficient in all cases. This efficiency is essential for continental-scale applications and is particularly important for real-time monitoring and nowcasting. It also supports the efficient production and iterative refinement of long-term historical products at high spatial and temporal resolution. Once the weights are determined, the analysis value at the target grid cell is computed using Eq. (1), yielding the optimal precipitation estimate.

Using the scaled weights w_i' from Eq (6), the uncertainty information in the blended field can be expressed either as the estimated error variance of the final analysis ($\overline{E_k^2}$) or as its normalised form ($\frac{\overline{E_k^2}}{f_k^2}$), as below:

$$\frac{\overline{E_k^2}}{f_k^2} = 1 - \sum_{i=1}^{n} w_i' \cdot (\mu_{ki} + \tau_{ki}\sigma_i) \quad (7)$$

This formulation shows how the analysis error is reduced according to the correlation between each observation and the background error at the target location, together with the associated observation error. Observations with stronger correlations and smaller errors contribute more to reducing the analysis uncertainty.

3.3 Local bias correction of satellite and radar precipitation estimations

Bias correction for satellite and radar data followed a Kalman filtering approach similar to that of Chumchean et al. (2006), but was adapted from the original mean-field framework to estimate spatially varying local bias fields at the target hourly timescale. Bias estimation was based on co-located satellite/radar–gauge pairs, obtained by extracting satellite or radar estimates at gauge locations and pairing them with the corresponding gauge observations. All available gauges were included in the satellite bias correction, whereas only gauges within radar coverage were included in the radar bias correction because radar estimates are unavailable outside the radar coverage area. Bias at each gauge location was estimated using a Kalman filter with an autoregressive model of order one (AR(1)) to capture temporal dependence, and the resulting point-based bias estimates were interpolated using ordinary kriging to generate a continuous spatially varying bias field. The corrected precipitation estimates were then obtained by applying the bias field multiplicatively to the raw precipitation estimates.

The calibrated radar estimates (R1) used in this study differ from the operational Rainfields product (R0) in both temporal and spatial configurations. R0 applies bias correction using gauges within a 150-km radius and a 15-min window. The spatial radius limits the number of nearby co-located radar–gauge pairs available for local bias estimation, while the temporal window is constrained by gauge reporting latency and the short operational update interval. In contrast, R1 uses gauges within a 300-km radius and a 1-hour window, increasing the number of radar–gauge pairs available for estimating the local radar bias. No predefined limit is imposed on the number of pairs within this radius. All available pairs are considered, with their point-scale bias estimates subsequently interpolated using ordinary kriging to construct a spatially continuous bias field. The larger spatial radius allows more spatially distributed gauge observations to be included, while the longer temporal window accommodates additional observations that become available after accounting for gauge reporting latency. This approach also uses the same set of available gauge observations for satellite and radar bias correction, subject to the availability of radar observations at each gauge location. However, this configuration is tailored to the Australian radar system and can be adjusted for other radar systems according to their operational configurations and production objectives.

3.4 Error characterisation

Error characterisation is essential for determining observation weights. It involves estimating the error variances and correlations of each data source for both gauged and ungauged locations. Ideally, this error analysis should be conducted at each target grid cell to obtain accurate error estimates.

For gauged locations, this task is relatively straightforward, as gauge observations can be used as a reference for estimating the error characteristics of the background and observation inputs. Although gridded satellite and radar products represent areal averages while gauges provide point measurements, the gauge network is generally too sparse to derive reliable areal-average estimates at the 2-km grid scale. Therefore, point gauge observations were used directly as the reference. At the 2-km spatial resolution adopted in this study, point-to-area representativeness differences were assumed to be sufficiently small and were not explicitly considered. Consequently, the estimated error characteristics should be interpreted as relative measures of uncertainty among different data sources rather than absolute estimates of their true errors.

For ungauged grid cells (99.9% of the national 2-km land grid cells), however, error characterisation becomes considerably more challenging. A common approach is to incorporate spatial and temporal windows to gather sufficient samples. For example, for a target grid cell, one might analyse data from preceding month to capture recent performance and include all available hourly gauges within a 10° × 10° longitude–latitude window to account for spatial variability. However, implementing such a strategy is impractical for the kilometre-scale national framework considered in this study. A 2-km resolution product over Australia comprises more than 5 million grid cells (including ocean areas of interest, see Fig. 1d). Furthermore, the sparse and highly uneven distribution of hourly gauges means that fixed spatial and temporal windows are generally unsuitable. Instead, the search windows would need to be adaptively adjusted for each grid cell and time step

according to local gauge availability to ensure sufficient samples, resulting in substantial computational costs, implementation complexity, and extensive parameter tuning.

To simplify the process, regional error characteristics were estimated by dividing the analysis domain into three subregions. Satellite errors showed a clear latitudinal dependence, with larger errors generally occurring in tropical northern Australia. In contrast, radar error characteristics are more radar-specific, with errors differing depending on local topography around the radar range, differences in the radar type and hardware configuration, and site-specific Z–R parameters. In addition, the bias correction of radar data helped reduce range-dependent error to some extent. Nevertheless, for simplicity and consistency in this first instance, the same regional divisions were applied to both satellite and radar error characterisation. Specifically, the Australian domain was divided into tropical, subtropical, and temperate subregions. Within each subregion, analytical functions describing error variances and error correlations were fitted using data from gauged locations, and the resulting error characteristics were subsequently applied to ungauged locations within the same subregion.

For error variance estimation, we calculated the squared differences between satellite (or radar) estimates and gauge observations. The error variance increases with precipitation intensity, making this relationship suitable for fitting error variance curves. To capture this, precipitation intensities were divided into bins, and within each bin, the mean squared error between satellite (or radar) estimates and gauge observations was calculated as an estimate of the error variance. This analysis showed that error variance is a function of precipitation intensity. Various analytical models were tested to represent the scatter, and the optimised parameters for the best-fitting curves were obtained.

For error correlation estimation, pairs of satellite (or radar) estimates and gauge observations were collected, and the error correlation was calculated for each pair along with their corresponding distance. Distances were similarly divided into bins, and within each bin, the mean error correlation was calculated. This revealed that error correlation is a function of distance. As with error variances, different analytical models were applied to the scatter, and the optimised parameters for the best-fitting curves were determined.

3.5 Evaluation strategies

The evaluation was designed primarily to assess the added value of integrating satellite, radar, and gauge observations within the BRAIN framework. The three-source satellite–radar–gauge analysis was therefore evaluated against individual-source fields and reduced-source blending configurations (i.e., satellite–gauge blending) to determine how the incorporation of additional observation sources affects analysis performance.

BRAIN was also compared with rainfall products and methods currently used operationally by the Bureau to provide additional operational context. Gauge-based IDW interpolation was included as a simple gauge-only reference because it is currently used in the Bureau's operational flood forecasting system to estimate catchment- and/or sub-catchment-scale rainfall from sub-daily gauge observations for hydrological modelling (Malone, 1999; Malone and Carroll, 2022), rather than

to generate a national sub-daily gridded rainfall product. AGCD was included as an existing national operational daily gridded rainfall product (Jones et al., 2009).

3.5.1 Evaluation datasets and cross-validation

Three gauge datasets were used to provide complementary evaluations of BRAIN. The primary hourly evaluation used the sub-daily gauge observations shown in Fig. 1a. A 20-fold cross-validation was conducted, in which the gauges were divided into 20 non-overlapping groups. For each fold, approximately 95% of the gauges were retained for blending, while the remaining 5% were withheld and used exclusively for validation. This procedure was repeated across all 20 folds so that each gauge was used once for validation. The same folds were applied to the gauge-based IDW interpolation to ensure a consistent comparison.

A separate daily gauge dataset (Fig. 1b), independent of the sub-daily gauges used for blending, was used for complementary evaluation at the daily scale. Hourly BRAIN estimates were converted from UTC to local time and accumulated to daily totals to match the daily gauge observation period. The resulting daily estimates were compared with these observations, providing an independent assessment at a longer accumulation timescale.

An additional independent hourly dataset comprising approximately 2000 gauges (see Fig. S13) was collated after the completion of the main analyses and used for supplementary evaluation. As these gauges were not used in either the bias correction or BRAIN blending processes, this dataset provides a further independent assessment of hourly performance and complements the primary cross-validation analysis.

3.5.2 Performance metrics and stratified evaluation

Performance was evaluated using three metrics: correlation, root mean square error (RMSE), and mean bias. Correlation measures the strength of the linear relationship between estimated and observed rainfall, with values closer to 1 indicating stronger agreement. RMSE measures the overall magnitude of the errors, with lower values indicating better accuracy. Mean bias measures systematic overestimation or underestimation, with values closer to zero indicating smaller systematic bias. These metrics were calculated separately for each gauge to characterise spatial variations in performance.

In addition to the overall evaluation, performance was examined across different rainfall intensities. At each gauge, observed rainfall was divided into three categories: low (from 0.2 mm h^{-1} for hourly data or 1 mm day^{-1} for daily data up to the 50th percentile), moderate (50th–90th percentile), and high (>90th percentile). Performance metrics were calculated separately for each rainfall-intensity category at each gauge. This analysis was used to examine how product behaviour varies with rainfall intensity.

Performance was also evaluated according to local gauge density to examine the influence of gauge availability. For each validation gauge and time step, gauge density was defined as the number of available gauges used for blending within a 200-km radius. Low- and high-density conditions were defined as gauge densities below the 25th percentile and above the 75th

percentile of the gauge-density distribution, respectively. Performance was then evaluated separately under these contrasting gauge-density conditions to assess the sensitivity of the blended analysis to gauge availability.

For all gauge-based evaluations, gridded estimates were matched to gauge locations using nearest-neighbour interpolation, whereby the value from the grid cell with the minimum Euclidean distance to each gauge location was selected. This approach preserves the values of the original gridded analyses and avoids additional spatial smoothing that may be introduced by interpolation methods such as bilinear interpolation. Nevertheless, comparisons between point-based gauge observations and grid-cell rainfall estimates are subject to inherent point-to-area representativeness differences, which should be considered when interpreting the evaluation results.

3.5.3 IDW implementation and comparison with AGCD

Gauge-based IDW interpolation was included as a simple gauge-only reference. The primary IDW configuration used the five nearest available gauges, selected according to Euclidean distance, with an inverse-distance weighing power of 2 and no maximum search distance. This configuration is referred to as IDW-K5 and is shortened to IDW in the main evaluation. To examine the sensitivity of the comparison to the IDW configuration, two additional configurations were considered. IDW-K5-L retained the five-gauge configuration of IDW-K5 but imposed a maximum search distance of 200 km, allowing the effect of the distance constraint to be examined. IDW-K20-L used up to 20 gauges within a 200-km radius, consistent with the gauge-selection configuration used in BRAIN. The sensitivity of the results to these IDW configurations is examined in Section 5.2.

At the daily scale, BRAIN was compared with AGCD, an existing national operational daily gridded rainfall product. AGCD is a 5-km gauge-based gridded analysis derived from daily gauge observations using an anomaly-based approach that combine Barnes successive-correction analysis with a climatological background (Jones et al., 2009). The daily gauge network used for AGCD is substantially denser than the sub-daily gauge network available to BRAIN. Hourly BRAIN estimates were accumulated to daily totals for comparison with AGCD. Daily BRAIN accumulation accounted for the conversion from UTC to local time to align with the 9 am to 9 am observation periods used by AGCD. However, half-hour time-zone offsets in some Australian regions and daylight saving time adjustments, meant that exact alignment could not always be achieved, potentially introducing minor temporal mismatches. These differences in input gauge networks, temporal resolution, accumulation periods, and product design should therefore be considered when interpreting the comparison between BRAIN and AGCD.

There are several existing global precipitation products (e.g., Beck et al., 2019; Ma et al., 2025) that could potentially be used for comparison with BRAIN. However, these products differ from BRAIN in their spatial and temporal resolutions, operational objectives, and observational inputs. In particular, BRAIN is designed as a high-resolution operational product for Australia with a target data latency of less than one hour and incorporates a large number of hourly gauge observations and regional radar data that are not generally used in global precipitation products. These differences should be carefully

considered in direct product comparisons. The current study therefore focuses on the development and evaluation of the BRAIN framework, including its performance relative to its constituent data sources and different blending configurations. We are currently working towards the development of a long-term BRAIN dataset, which will enable more systematic comparisons with existing global precipitation products. Such comparisons will also provide an important opportunity to assess the potential benefits of incorporating regional observational datasets.

4 Results

4.1 Satellite and radar bias correction

Figure 3 demonstrates the spatial patterns and statistical improvements in mean bias for satellite and radar precipitation estimates after bias correction, evaluated against hourly gauge observations across Australia over 2022–2023 period.

Before correction, satellite data exhibit a clear latitude-dependent bias pattern, with notable overestimation in tropical regions, which decreases progressively towards subtropical and temperate regions (Fig. 3a; see also Fig. S1a). The corresponding histogram (Fig. 3e) reveals a highly positive-skewed distribution, indicating substantial overestimation across most hourly gauges. After correction, biases (Fig. 3b) are significantly reduced where initial errors were large, and the bias distribution (Figs. 3f and S1c) becomes narrower and more symmetric.

For radar data, the operational Rainfields product shows no clear latitude-dependent bias but exhibits localised errors, particularly along the east coast (R0, Fig. 3c; see also Fig. S1b). The histogram (Fig. 3g) indicates a general tendency toward overestimation. After applying the bias correction used in this study (R1, Fig. 3d), the spatial distribution of biases become more consistent, and large biases are reduced. The error distributions (Figs. 3h and S1d) become more symmetric and centred around zero.

These results highlight the importance of bias correction as a critical pre-processing step to reduce systematic errors and improve the quality of inputs for blending.

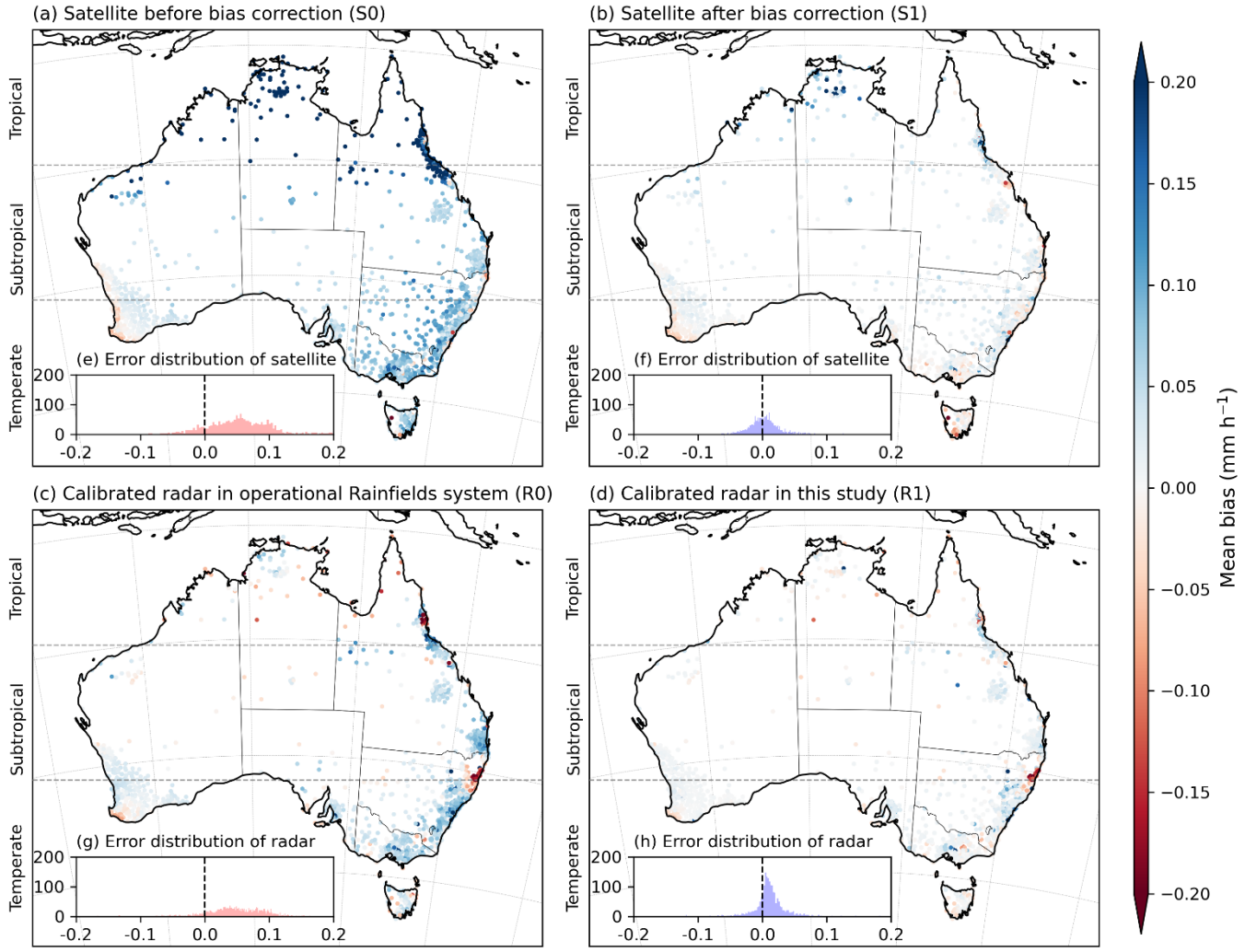


Figure 3. Spatial distribution of mean bias (mm h^{-1}) for (a, b) satellite precipitation before (S0) and after (S1) bias correction, and (c, d) radar precipitation calibrated using the operational Rainfields system (R0) and the method in this study (R1). The operational Rainfields calibration (R0) uses sub-daily gauges within a 150-km radius and a 15-min time window, whereas the calibration in this study (R1) uses a 300-km radius and a 1-hour time window. The analysis includes all available hourly gauges from 2022 to 2023. Histograms illustrate the error distributions across all hourly gauges for the corresponding datasets, with the dashed line marking zero bias. The boundaries of the tropical, subtropical, and temperate subregions used in the regional analysis are indicated in each panel. Note that fewer gauges are shown for radar because gauges outside radar coverage are excluded. An extended analysis across different subregions is provided in Fig. S1 of the Supplement.

4.2 Error characterisation

Figure 4 presents a subregion-dependent analysis of error variance and error correlation for satellite and radar products. Figure 4a shows that error variance increases approximately quadratically with precipitation intensity for both products. Satellite data have higher error variance than radar data across all intensities, especially in tropical regions, where the fitted curve is steepest. Radar consistently shows lower error variance, reflecting its generally higher accuracy and supporting the assignment of greater weights to radar observations in blending. The constant term of the quadratic fit was fixed to ensure an approximate 2:1 error variance ratio between satellite and radar. To account for gauge errors, the error variance of each gauge was defined as the precipitation intensity plus one. This parameterisation was based on empirical estimates from Xie and Xiong (2011), given the limited availability of sub-daily gauge data in Australia.

Figure 4b shows that satellite error correlation declines exponentially with distance, with a similar pattern observed across all subregions. Tropical areas exhibit the highest short-range correlations, followed by subtropical and temperate regions. Only satellite error correlations are shown, as radar–radar and radar–gauge correlations were not considered in the blending framework. These results highlight region-specific error characteristics. The quadratic relationship with intensity underscores the need for intensity-dependent error variance estimation, while the exponential decay in correlation reflects the spatially localised nature of precipitation errors.

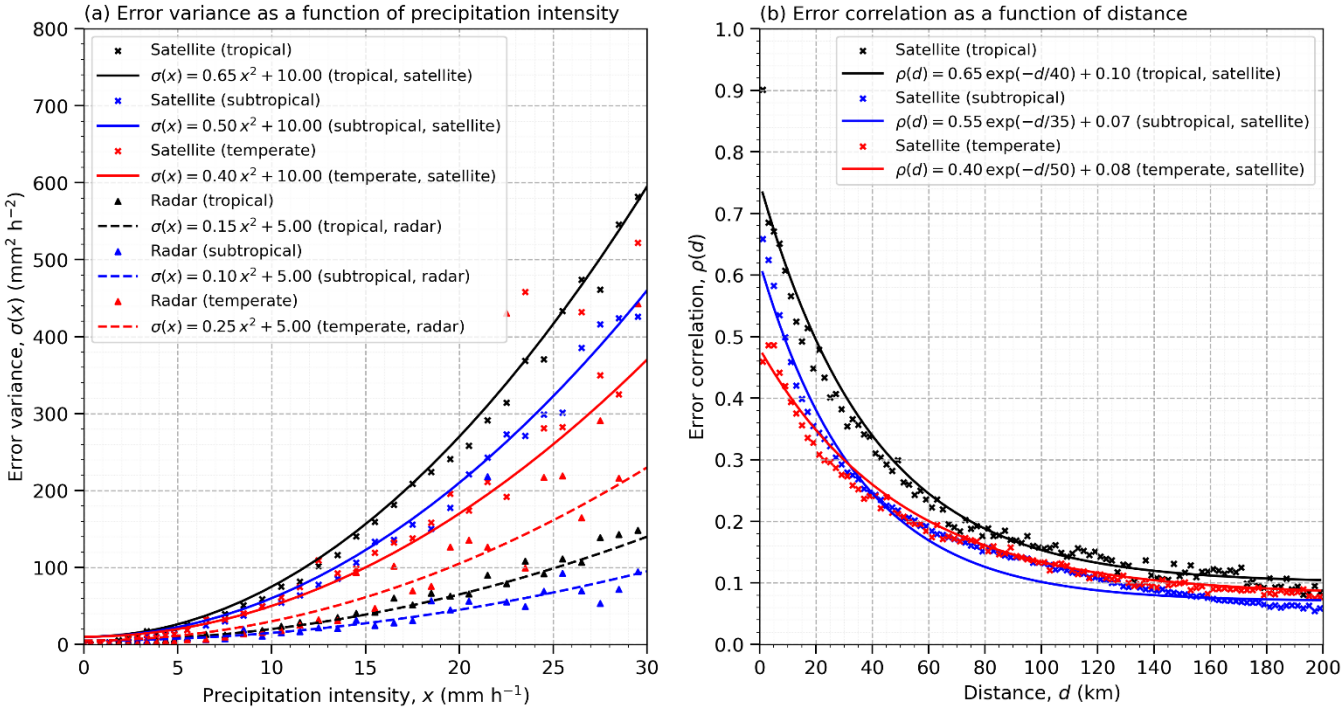


Figure 4. Estimated error characteristics of satellite and radar precipitation estimates across tropical, subtropical, and temperate regions. (a) Error variance as a function of precipitation intensity, with quadratic functions fitted separately for

each data source and region. (b) Satellite error correlation as a function of distance, with exponential decay functions fitted separately for each region. Radar error variance in different zones does not fully reflect the spatial characteristics of individual radars, as their errors are more radar-specific. For simplicity, we grouped radars within the same subregions and derived the error variance curves accordingly.

4.3 Evaluation

4.3.1 Comparison with individual data sources

The overall performance of the blended rainfall product (BR-SRG) was first compared with that of the individual satellite, radar and simple gauge-based IDW interpolation using the hourly-gauge 20-fold cross-validation and the independent daily-gauge evaluation. The performance distributions are presented as box plots in Figs. 5 and 6, respectively. Comparisons were conducted separately within and outside radar coverage, as radar estimates are unavailable at gauges outside the radar domain. Corresponding spatial comparisons among S1, R1, IDW, and BR-SRG are provided in the Supplement for the hourly-gauge cross-validation (Figs. S5–S7) and independent daily-gauge evaluation (Figs. S8–S10), showing correlation, RMSE, and mean bias, respectively.

Within radar coverage, where all estimates could be compared consistently and sufficient validation samples were available, performance was further examined across different rainfall intensities using the hourly-gauge 20-fold cross-validation (Fig. 7). Corresponding results from the independent daily-gauge evaluation are provided in the Supplement (Fig. S3).

Results from the additional independent hourly-gauge evaluation are also provided in the Supplement, including overall performance distributions (Fig. S16) and spatial comparisons among S1, R1, IDW, and BR-SRG in terms of correlation, RMSE, and mean bias (Figs. S17–S19, respectively). The corresponding rainfall-intensity analysis is presented in Fig. S20.

Comparison with the satellite estimates. BR-SRG showed consistently higher correlations, lower RMSE, and smaller biases than both the original satellite product (S0) and its bias-corrected version (S1). In the hourly cross-validation, these improvements were evident both within and outside radar coverage (Fig. 5), although the differences were greater within radar coverage. Similar improvements were observed in the independent daily-gauge (Fig. 6) and independent hourly-gauge evaluations (Fig. S16). The rainfall-intensity analysis further showed that BR-SRG maintained higher correlations, generally lower RMSE, and smaller biases than S0 and S1 across low-, moderate-, and high-intensity rainfall categories within radar coverage (Fig. 7). Similar intensity-dependent differences were observed in the independent daily-gauge (Fig. S3) and independent hourly-gauge evaluations (Fig. S20).

Comparison with the radar estimates. The bias-corrected radar product (R1) showed strong overall performance within radar coverage. In the hourly-gauge cross-validation, R1 had slightly higher correlation and lower RMSE than BR-SRG, whereas BR-SRG showed a smaller absolute bias (Fig. 5). In contrast, BR-SRG generally showed higher correlation, lower RMSE, and smaller absolute bias than R1 in both the independent daily-gauge (Fig. 6) and independent hourly-gauge (Fig.

S16) evaluations. The rainfall-intensity analysis provided further insight into these differences. BR-SRG generally performed better than R1 in terms of correlation and RMSE at low and moderate rainfall intensities, whereas R1 performed better at high rainfall intensities. For bias, however, R1 generally showed a less negative bias than BR-SRG across all rainfall-intensity categories, with the difference becoming more evident at high intensities (Figs. 7, S3 and S20).

The more negative bias of BR-SRG relative to R1 at high rainfall intensities may result from the blending process. Radar estimates can better capture localised intense rainfall, whereas incorporating satellite estimates may smooth rainfall peaks in some cases. However, the effects of blending vary between rainfall events, as further illustrated by the selected case studies in Section 5.3.

The negative biases observed for both R1 and BR-SRG at high rainfall intensities should also be interpreted with caution for two reasons. First, rainfall-intensity categories were defined using gauge observations, which may introduce conditional sampling bias. For example, cases where gauges record heavy rainfall but gridded estimates are lower are included in the high-intensity category, whereas cases where gridded estimates indicate heavy rainfall but gauges record lower intensities are assigned to lower-intensity categories. This sampling effect may contribute to the negative biases observed at high observed rainfall intensities. Second, gauges provide point measurements, whereas R1 and BR-SRG represent gridded rainfall estimates. Differences in spatial representativeness may also contribute to the observed negative biases, particularly for highly localised rainfall events.

Comparison with IDW interpolation. Within radar coverage, BR-SRG showed substantially higher correlations and lower RMSE than IDW in the hourly-gauge cross-validation (Fig. 5a, c). Similar differences were observed in the independent daily-gauge evaluation (Fig. 6a, c) and were further supported by the independent hourly-gauge evaluation (Fig. S16a, c). The rainfall-intensity analysis provided further evidence of these differences, with BR-SRG generally maintaining higher correlations and lower RMSE than IDW across all intensity categories (Figs. 7, S3 and S20). Outside radar coverage, BR-SRG maintained higher correlations than IDW in both the hourly-gauge and daily- gauge evaluations (Figs. 5b, 6b and S16b). BR-SRG also showed lower RMSE in the hourly-gauge evaluation (Figs. 5d and S16d), whereas its RMSE was slightly higher than that of IDW in the daily evaluation (Fig. 6d). In terms of bias, however, IDW generally showed smaller absolute biases than BR-SRG in both the hourly and daily evaluations (Figs. 5f, 6f and S16f). The possible reasons for the performance differences between BR-SRG and IDW are discussed in Section 5.2.

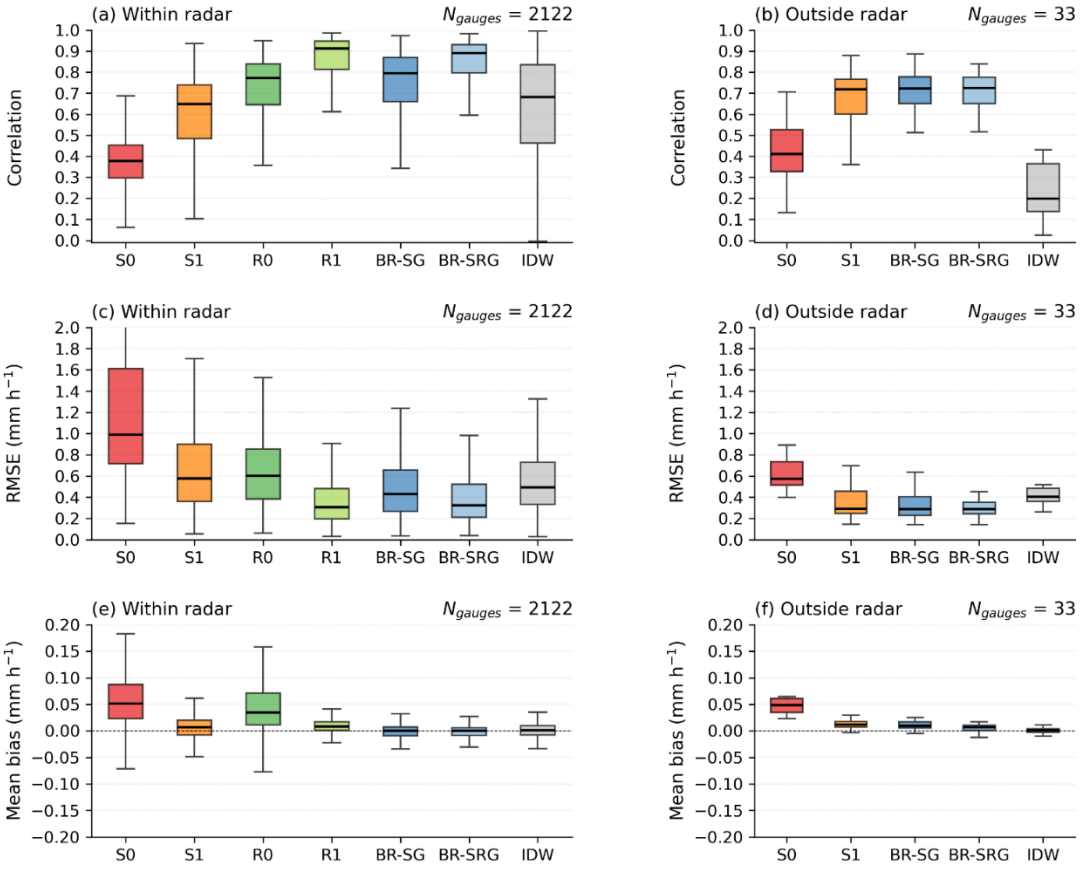


Figure 5. Performance of different rainfall estimates in the hourly-gauge 20-fold cross-validation, shown separated for evaluation gauges (a, c, e) within radar range and (b, d, f) outside radar range (see Fig. 1a). Panels show correlation (a, b), RMSE (c, d), and mean bias (e, f). Higher correlation, lower RMSE, and bias closer to zero indicate better performance. Products include raw satellite (S0), bias-corrected satellite (S1), original radar (R0), bias-corrected radar (R1), two-source blend (BR-SG; BRAIN with satellite and gauge), three-source blend (BR-SRG; BRAIN with satellite radar and gauge), and gauge-based interpolation (IDW). In each fold, hourly gauges for evaluation were selected without replacement.

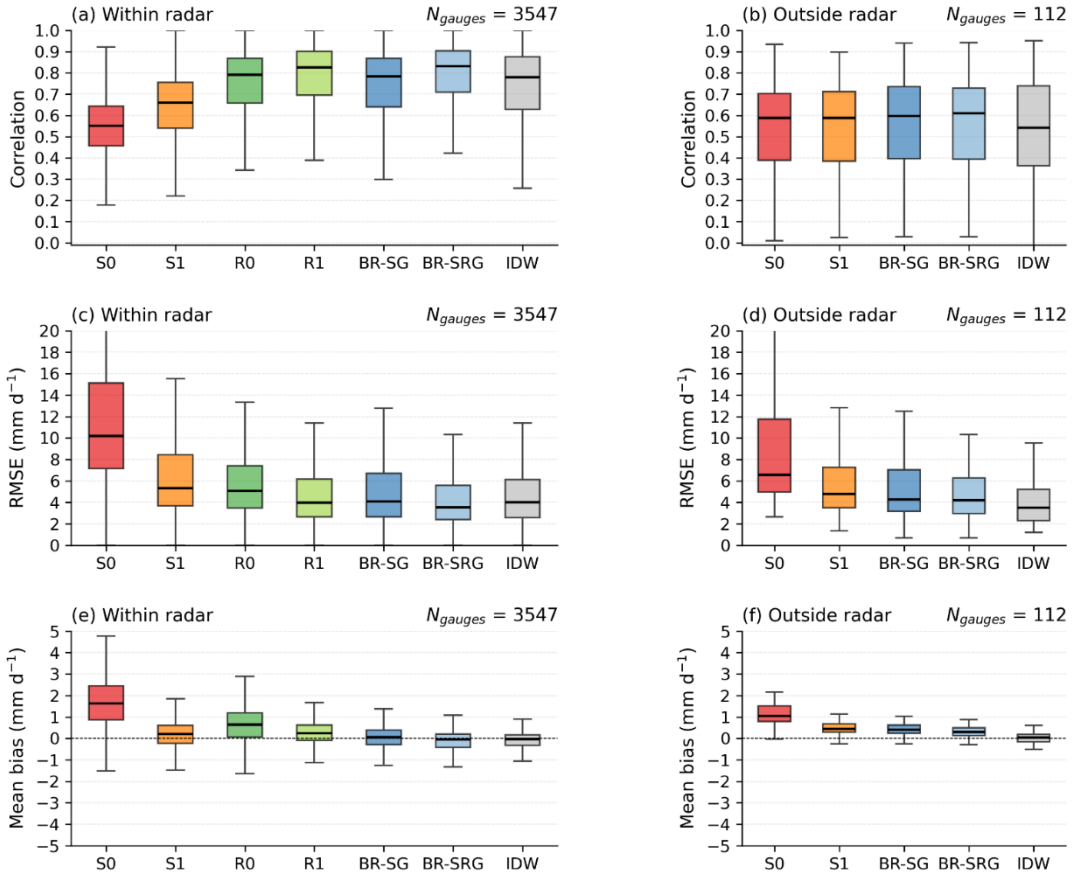


Figure 6. Performance of different rainfall estimates in the independent daily-gauge evaluation, shown separately for evaluation gauges (a, c, e) within and (b, d, f) outside radar coverage (see Fig. 1b). Panels show (a, b) correlation, (c, d) RMSE, and (e, f) mean bias. Higher correlation, lower RMSE, and mean bias closer to zero indicate better performance. The evaluated rainfall estimates include the raw satellite estimate (S0), bias-corrected satellite estimate (S1), original radar estimate (R0), bias-corrected radar estimate (R1), two-source satellite–gauge blend (BR-SG), three-source satellite–radar–gauge blend (BR-SRG), and gauge-based IDW interpolation.

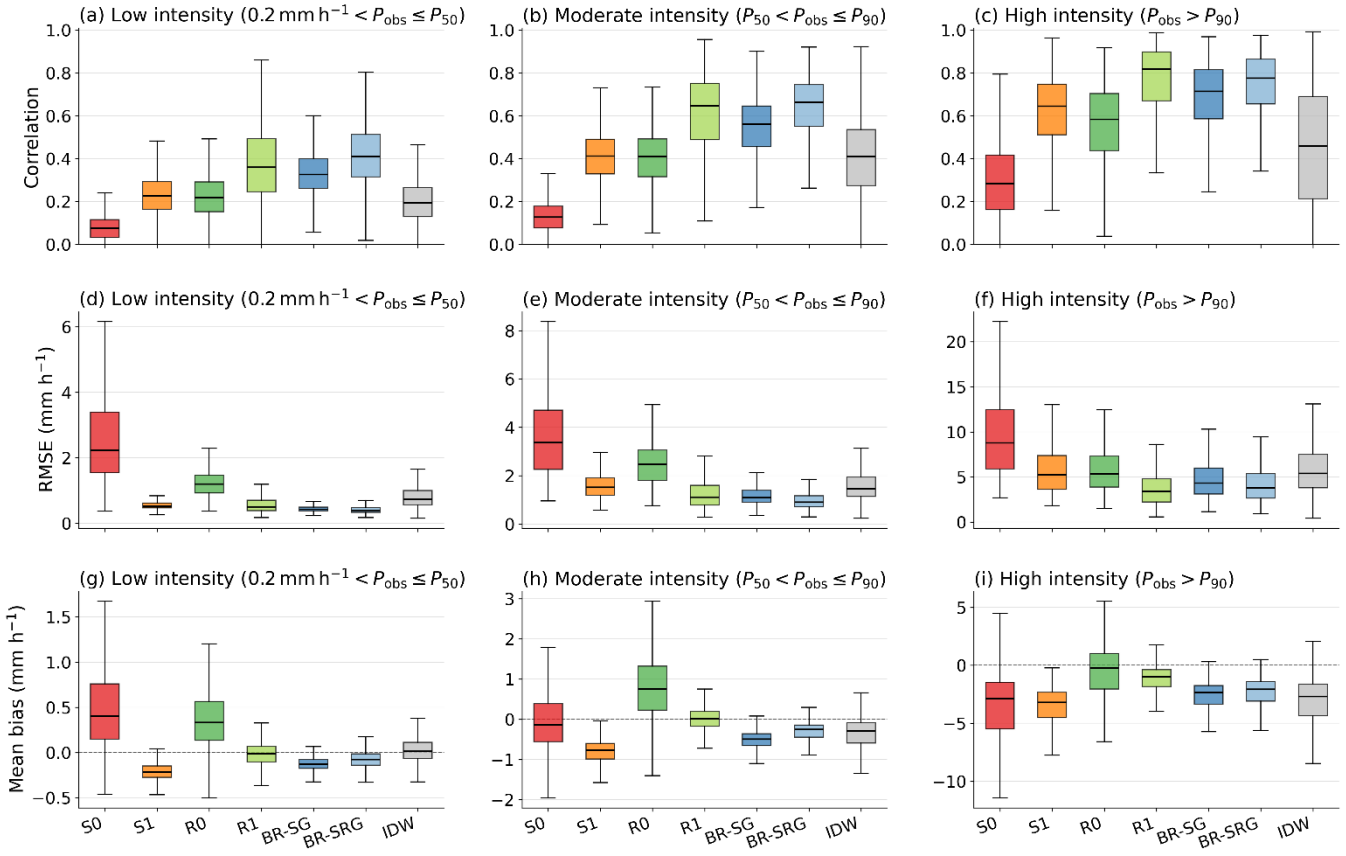


Figure 7. Performance of different rainfall estimates across rainfall-intensity categories in the hourly-gauge 20-fold cross-validation. At each gauge, observed rainfall was divided into three categories: low (0.2 mm h^{-1} < *P*obs ≤ *P*50), moderate (*P*50 < *P*obs ≤ *P*90), and high (*P*obs > *P*90), where *P*50 and *P*90 are the 50th and 90th percentiles of observed rainfall above 0.2 mm h^{-1} at each gauge, respectively. Panels show (a–c) correlation, (d–f) RMSE, and (g–i) mean bias. Each box represents the distribution of station-based metrics across gauges. As the rainfall-intensity categories are defined based on observations, the mean bias for these categories should be interpreted with caution, particularly for high-intensity rainfall, where observation-based stratification can contribute to a tendency towards negative conditional bias.

4.3.2 Comparison of three-source and two-source blending

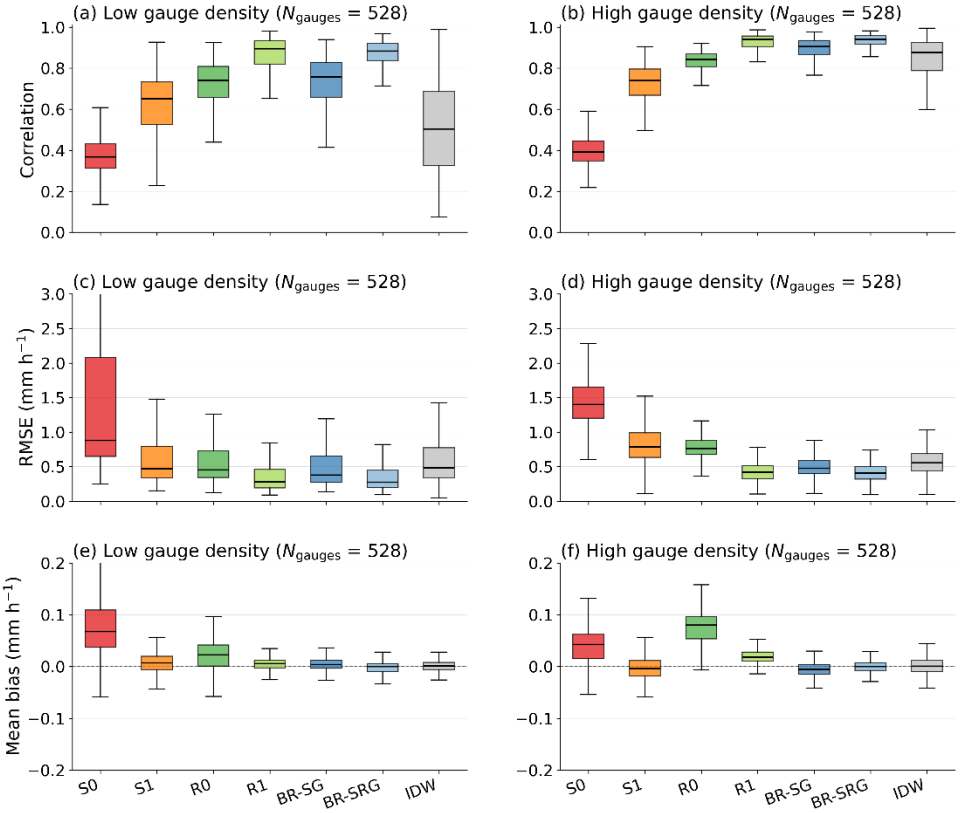
The three-source blended product (BR-SRG; satellite–radar–gauge) was also compared with the two-source combination (BR-SG; satellite–gauge) to assess the additional contribution of radar observations. Within radar coverage, BR-SRG consistently showed higher correlations and lower RMSE than BR-SG in the hourly-gauge cross-validation (Fig. 5). Similar improvements were observed in the independent daily-gauge evaluation (Fig. 6) and were further supported by the independent hourly-gauge evaluation (Fig. S16). Differences in mean bias were comparatively small, with both products

generally showing biases close to zero in the overall evaluations. The rainfall-intensity analysis further showed that BR-SRG generally maintained higher correlations and lower RMSE than BR-SG across low, moderate, and high rainfall intensities (Figs. 7, S3 and S20). However, both products showed increasingly negative biases with increasing rainfall intensity. Outside radar coverage, differences between BR-SRG and BR-SG were smaller than those observed within radar coverage (Figs. 5, 6 and S16). Nevertheless, BR-SRG maintained better overall performance, with generally higher correlations, lower RMSE, and smaller absolute biases than BR-SG. This improvement suggests that nearby radar observations can provide useful additional information to the blended estimates beyond the radar coverage.

4.3.3 Performance under different gauge-density conditions

Gauge-density effects were examined using the hourly-gauge 20-fold cross-validation (Fig. 8). The analysis was restricted to areas within radar coverage because radar observations are unavailable outside these areas and the gauge network is generally too sparse for a meaningful comparison between gauge-density conditions. First, gauge density affected the magnitude of performance but did not change the overall relative performance among the rainfall estimates. BR-SRG consistently achieved the best overall performance under both low- and high-density conditions. Second, the influence of gauge density was most evident in correlation, which generally increased under high-density conditions across the gauge-dependent estimation processes. Changes in RMSE and mean bias were less consistent, likely reflecting differences in rainfall characteristics between the low- and high-density regions in addition to gauge-density effects. This density dependence was particularly pronounced for gauge-only IDW interpolation, which showed substantially lower and more variable correlations under low-density conditions but much higher and more consistent correlations under high-density conditions. Notably, however, its mean bias remained close to zero under both low- and high-density conditions.

The relative performance of the rainfall estimates remained consistent across all three evaluation datasets. BR-SRG maintained the best overall performance under both low- and high-density conditions in the independent daily-gauge (Fig. S4) and independent hourly-gauge (Fig. S21) evaluations, confirming that the overall ranking was robust to variations in gauge density. The improvement from low- to high-density conditions was more evident in these independent evaluations, further highlighting the importance of gauge availability for precipitation bias correction, multi-source blending, and gauge-based interpolation.



720 **Figure 8.** Performance of different rainfall estimates under low- and high-gauge-density conditions in the hourly-gauge 20-fold cross-validation, considering evaluation gauges within radar coverage only. Low- and high-density conditions correspond to the lower (≤25th percentile) and upper (≥75th percentile) tails of the gauge-density distribution, respectively, with gauge density defined as the number of available gauges within a 200-km radius. Panels show (a, b) correlation, (c, d) RMSE, and (e, f) mean bias. Each box represents the distribution of station-based metrics across 528 gauges.

725 **4.4 Spatial and temporal performance of the blended product**

Figure 9 shows the spatial performance of the blended product (BR-SRG) in terms of correlation and RMSE metrics evaluated against hourly gauge observations using the 20-fold cross-validation. High correlations were observed across most regions, particularly where gauge density is higher (Fig. 9a–c). RMSE was generally lower in coastal and well-observed areas, with higher values in regions with sparse gauges or greater rainfall variability (Fig. 9d–f). Some outliers may be 730 attributed to imperfect gauge quality control or residual errors in satellite and radar inputs (e.g., Fig. S6; see also Figs. S9 and S18). Performance estimates may also be affected by limited gauge records, such as those from gauges operating during wet seasons.

Additional spatial performance maps based on independent daily-gauge (Fig. S11) and hourly-gauge (Fig. S22) evaluations are presented in the Supplement. Monthly variations in performance at both hourly and daily scales are also presented in Fig. S12 in the Supplement. Overall, BR-SRG demonstrated good performance across Australia, with room for improvement in sparsely gauged regions.

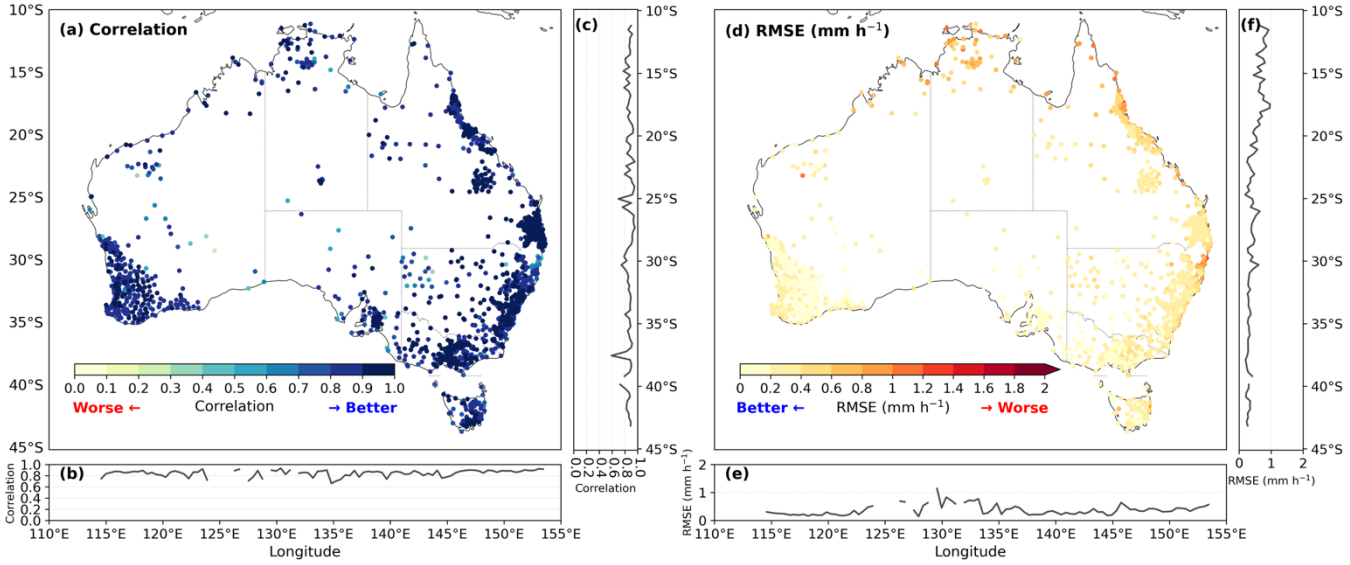


Figure 9. Spatial performance of the blended estimate (BR-SRG) evaluated against hourly gauge observations across Australia. Panels show the spatial distributions of (a) correlation and (d) RMSE (mm h^{-1}), with higher correlation and lower RMSE indicating better performance. Panels (b, e) and (c, f) show the corresponding longitudinal and latitudinal variations, respectively, averaged across gauges.

4.5 Demonstration of BRAIN in selected rainfall events

Figure 10 demonstrates the spatial characteristics of the hourly blended product (BR-SRG) for two selected extreme precipitation events, alongside the AGCD daily product and hourly gauge-based IDW interpolation: a 24-h accumulation during Cyclone Ellie from 22:00 UTC on 22 December to 22:00 UTC on 23 December 2022, and a 24-h accumulation during Cyclone Jasper from 22:00 UTC on 12 December to 22:00 UTC on 13 December 2023. The corresponding satellite and radar estimates are shown in Fig. S13. Hourly and daily gauge observations are shown in Fig. S14. The highest daily rainfall accumulations recorded by sub-daily and daily gauges during Cyclone Ellie and Cyclone Jasper are summarised in Tables S1 and S2, respectively.

Both satellite and radar captured the major rainfall systems associated with the two events, with satellite providing spatially continuous information across Australia and radar providing additional high-resolution information within its coverage. By integrating these spatially distributed estimates with gauge observations, BR-SRG captured the broad-scale rainfall patterns

while retaining finer-scale spatial structures and variations in precipitation intensity that were less evident in AGCD and IDW.

The representation of the most intense rainfall, however, depended on how well the different observations captured the rainfall maxima. During Cyclone Ellie, satellite (Fig. S13a) and radar (Fig. S13b) both identified substantial rainfall over northern Australia, but the highest rainfall occurred in an area with relatively sparse hourly gauge observations (Fig. S14a). Only one hourly gauge recorded a 24-h accumulation exceeding 100 mm (168.2 mm), while the next highest accumulation was 51.4 mm (Table S1). In comparison, the denser daily gauge network (Fig. S14b) provided multiple observations of high rainfall, including accumulations of 208.0, 184.6, and 141.4 mm (Table S1). The limited sampling of the rainfall maximum by hourly gauges therefore constrained the observational information available to BR-SRG (Fig. 10a) for representing the highest rainfall centre, whereas the additional daily observations provided stronger constraints for AGCD (Fig. 10b).

During Cyclone Jasper, satellite (Fig. S13c) and radar (Fig. S13d) clearly captured the intense rainfall system, with several hourly gauges located within the heavy rainfall centre and recording high rainfall accumulations (Fig. S14c). The highest hourly-gauge-derived 24-h accumulations reached 479.2, 456.5, and 378.4 mm (Table S2). The combination of spatially distributed satellite and radar estimates with these high-rainfall gauge observations enabled BR-SRG (Fig. 10d) to better represent the extreme rainfall than in the Cyclone Ellie case (Fig. 10a).

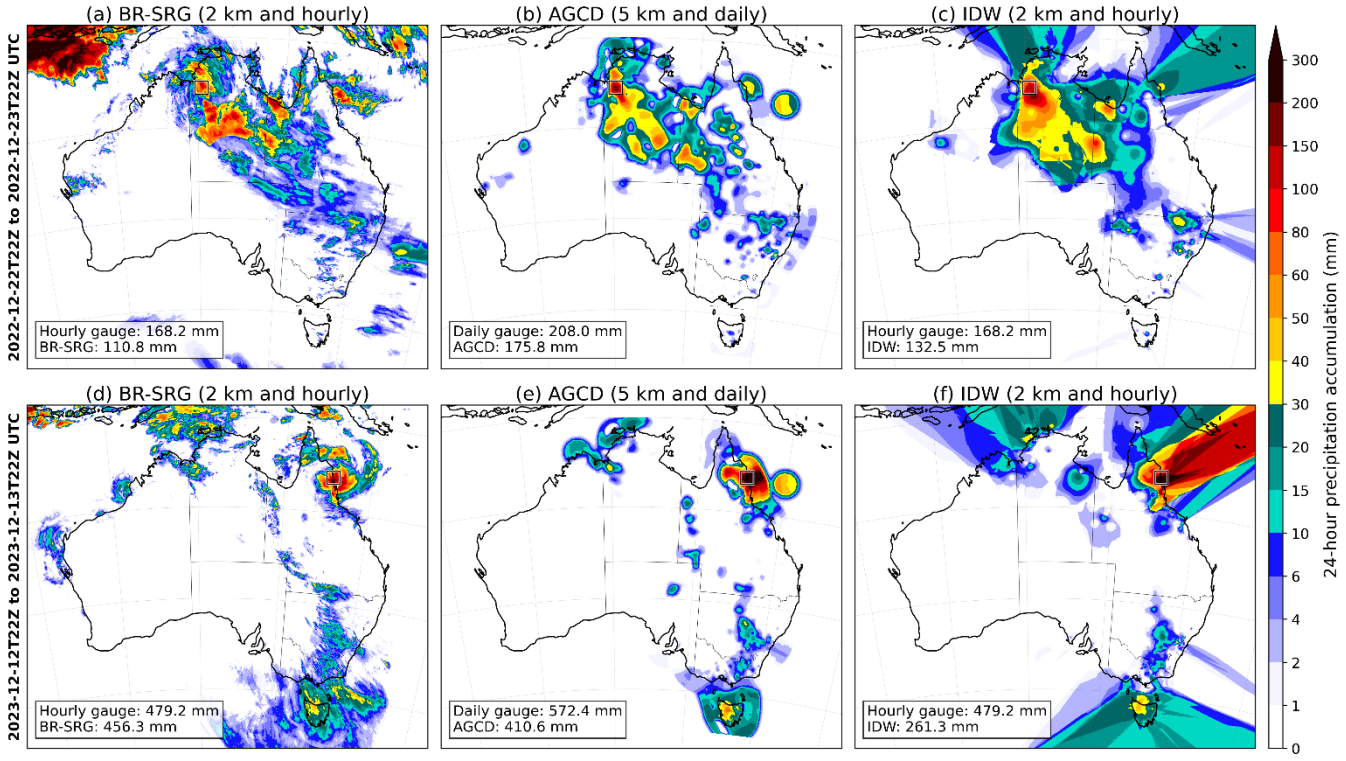


Figure 10. Example rainfall analyses from the three-source blend (BR-SRG; 2-km and hourly), AGCD (5-km and daily), and gauge-based IDW interpolation (2-km and hourly) for two selected 24-h periods during extreme precipitation events: (a–c) Cyclone Ellie, from 22:00 UTC on 22 December to 22:00 UTC on 23 December 2022, and (d–f) Cyclone Jasper, from 22:00 UTC on 12 December to 22:00 UTC on 13 December 2023. Note that AGCD incorporates the denser daily-gauge network (e.g., Fig. S14b, d), whereas BR-SRG and IDW use the comparatively sparser hourly-gauge network (Fig. S14a, c). BR-SRG and IDW are accumulated over the indicated UTC periods, whereas AGCD represents the standard daily gauge accumulation period of approximately 9 am to 9 am local time, ending on 23 December 2022 and 14 December 2023, respectively, with the exact UTC period varying across Australian time zones. The red square indicates the location of the gauge with the highest observed 24-hour precipitation for each event. Further details of the satellite and radar estimates and gauge observations are provided in Figs. S13 and S14 and Tables S1 and S2.

5 Discussion

5.1 Methodological contributions of the BRAIN framework

Multi-source blending of satellite, radar, and gauge precipitation observations using bias correction and statistical interpolation is not a new concept (e.g., Gandin, 1965; Xie and Xiong, 2011, Yu et al., 2020, Xia et al., 2025), but the BRAIN framework differs from previous approaches in several aspects of its implementation.

First, BRAIN was designed for computationally efficient application over a continental-scale domain such as Australia at high spatial and temporal resolution. The nearest-radar-point approximation within the localisation strategy substantially reduces the dimensionality of the statistical interpolation problem while retaining the source-specific error characterisation (Zhang et al., 2026), differing from the more computationally intensive formulation used in UKGrsHP (Yu et al., 2020).

BRAIN also uses a single satellite product as the spatially continuous background, with radar incorporated as an additional observation together with gauge observations. This differs from approaches that first combine satellite and radar to construct a blended background field for subsequent statistical interpolation with gauge observations (e.g. Xia et al., 2025). Because statistical interpolation requires characterisation of the spatial error structure of the background field, such pre-blending produces a new background whose error characteristics may differ from those of the original satellite and/or radar products. By retaining satellite and radar as separate sources, BRAIN allows their respective error characteristics and contributions to be explicitly represented within the statistical interpolation framework.

A further distinctive feature is that radar information is not restricted by a hard coverage mask. For each target location, BRAIN searches for the nearest available radar observation within a predefined maximum distance (200 km in this study). Consequently, radar information can still contribute to the blended estimate when the target location lies outside radar coverage, provided that a sufficiently close and reliable radar observation is available. Its effective contribution is determined by both the distance-dependent error correlation (Fig. 4b) and the estimated error variance, with greater weight

generally assigned to observations that are closer to the target location and have lower estimated errors. Even when the nearby radar estimate is not more accurate than the local satellite estimate on its own, it can provide complementary information that can improve the resulting estimate after blending.

This formulation allows radar information to contribute both within and near radar-covered regions, providing a gradual transition across radar-coverage boundaries while retaining the satellite estimate as the spatially continuous background. This differs from simple radar extrapolation, in which rainfall information within the radar domain is spatially extended into areas without radar observations. In BRAIN, the radar field itself is not extrapolated. The satellite estimate remains the background at every target location, while available radar and gauge observations contribute through the statistical interpolation according to their estimated error characteristics and spatial correlations.

5.2 Behaviour and sensitivity of gauge-based interpolation

The evaluation revealed two notable behaviours of IDW: its mean error (ME, or mean bias) remained consistently close to zero despite relatively large RMSE and lower correlation (Figs. 5 and S16), while its relative performance improved from hourly to daily evaluation, achieving a lower RMSE than BR-SRG at the daily timescale (Fig. 6), a pattern consistently observed across different subregions outside radar coverage (Fig. S2). To examine these behaviours, we compared the station-level contributions of positive and negative errors (Figs. 11, S24, and S25). The median positive-error contribution of IDW remained close to 0.5 across all three evaluations despite relatively large MAE (mean absolute error), indicating nearly equal contributions from positive and negative errors. At the hourly scale, this balance results in a near-zero ME despite relatively large individual errors, as reflected by the MAE and RMSE. The near-zero ME of IDW therefore primarily reflects error cancellation rather than uniformly small estimation errors. When hourly precipitation is accumulated to daily totals, these opposing errors can further offset over time, reducing the accumulated daily errors and contributing to the improved relative performance of IDW at the daily timescale (Figs. 6 and S24).

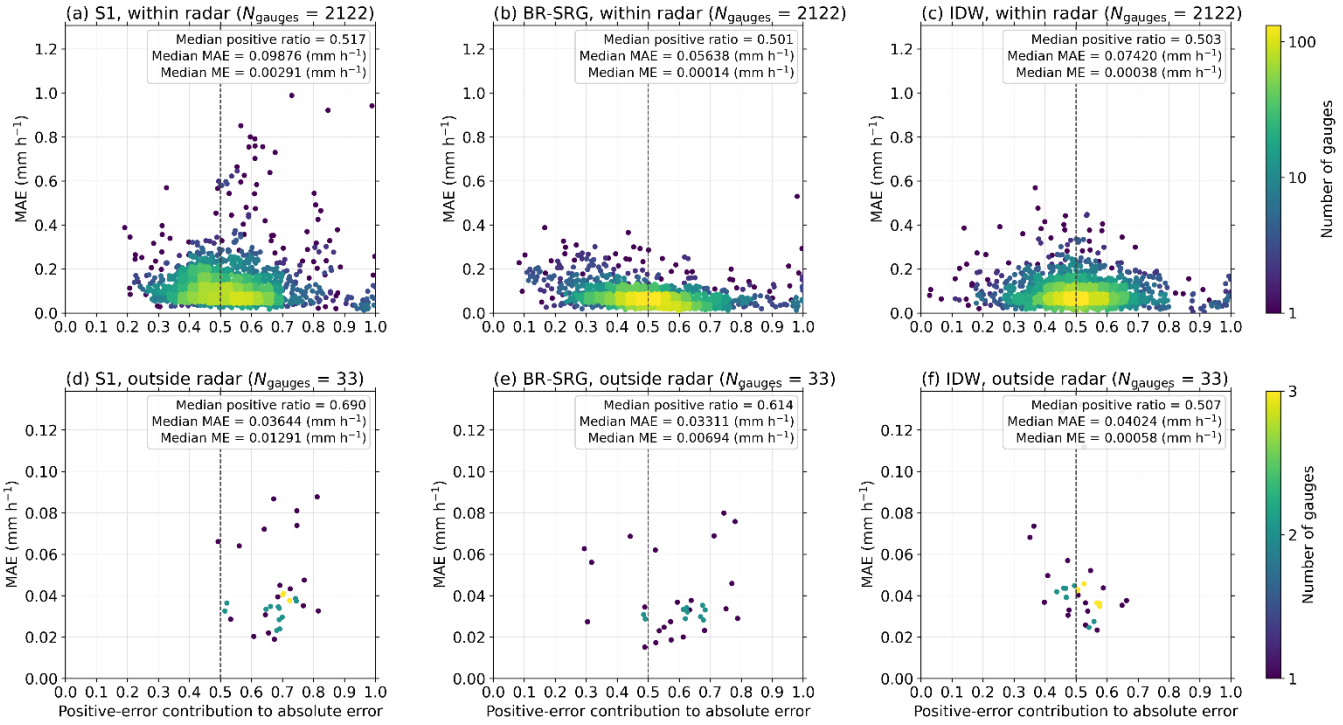


Figure 11. Relationship between positive-error contribution and mean absolute error (MAE) across evaluation gauges in the hourly-gauge 20-fold cross-validation for S1, BR-SRG, and IDW, evaluated (a–c) within and (d–f) outside radar coverage. Each point represents an individual gauge. Positive-error contribution is defined as the magnitude of positive errors relative to the total absolute error, such that a value of 0.5 indicates equal contributions from positive and negative errors. The vertical dashed line marks this balance point.

The sensitivity of IDW (Fig. 12) to its interpolation configuration was further examined using the same rainfall cases (Fig. 10). IDW-K5 provides a continuous field but can extend gauge influence over long distances in gauge-sparse regions. Applying a maximum search distance (IDW-K5-L) avoids such long-range interpolation but produces isolated rainfall patterns and areas without estimates, while increasing the number of gauges (IDW-K20-L) provides only limited improvement. Despite these differences, all configurations strongly smooth the rainfall field and poorly represent its spatial structure, particularly in gauge-sparse regions. These limitations are more evident in the spatial case studies than in the point-based validation above, which evaluates performance only at gauge locations.

More sophisticated gauge-based interpolation methods, such as thin-plate spline (TPS) (Nguyen et al., 2026) (Fig. 13), can improve spatial continuity but remain constrained by sparse gauge observations, with local rainfall features being overly smoothed and estimates becoming increasingly unreliable far from available gauges.

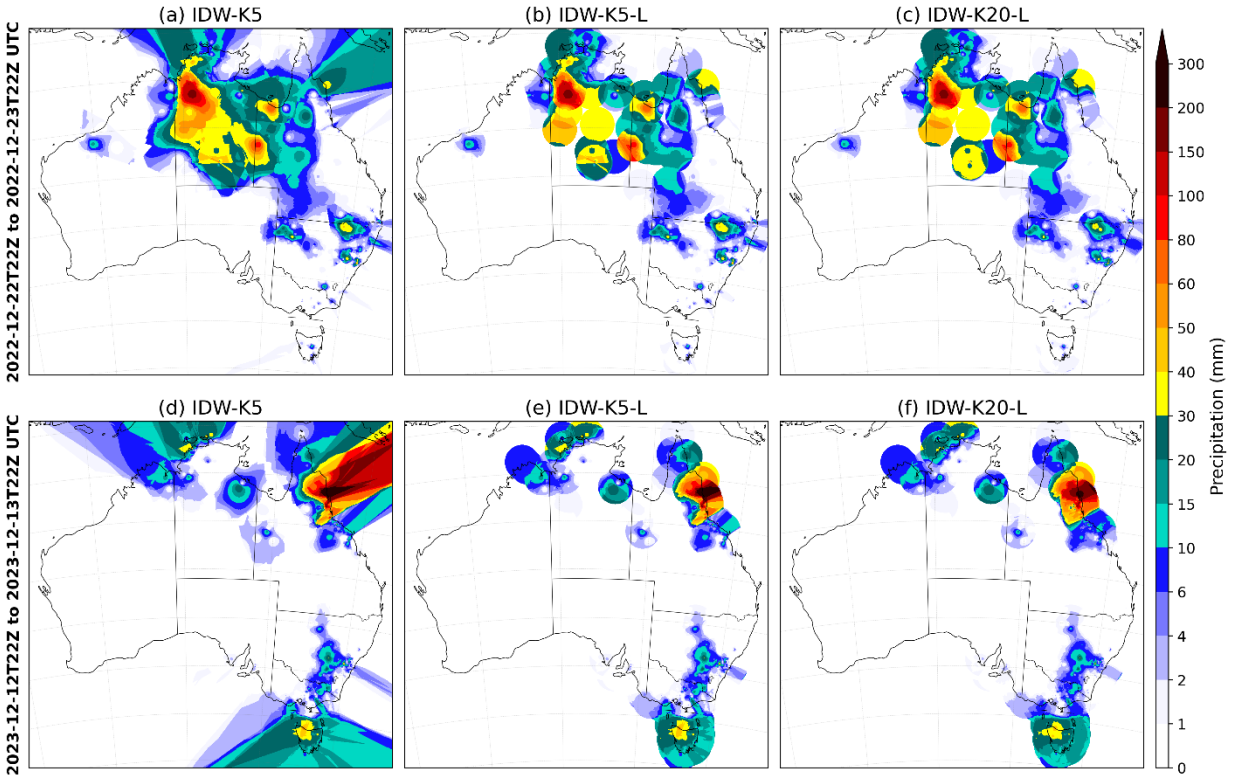
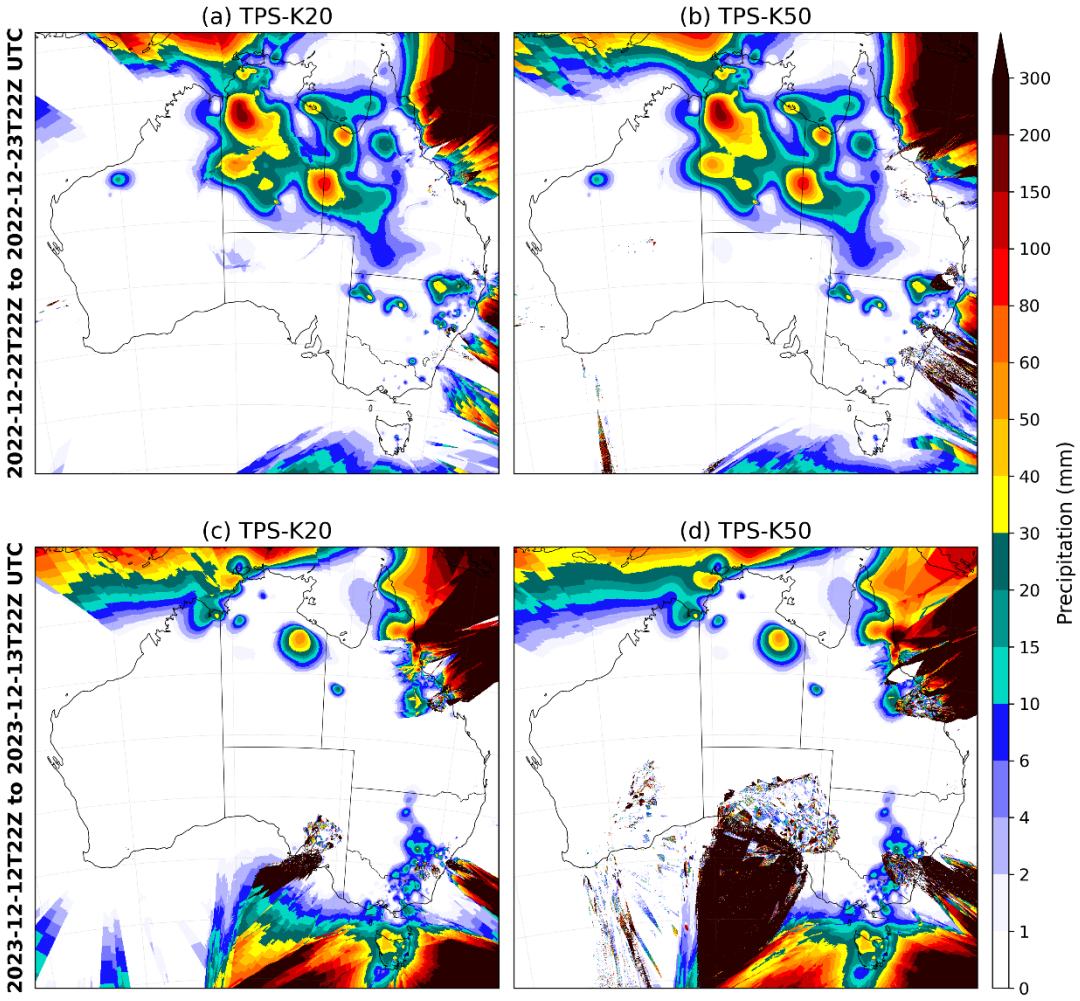


Figure 12. Sensitivity of 24-h accumulated precipitation estimates to different IDW configurations for two selected extreme precipitation events: (a–c) Cyclone Ellie, from 22:00 UTC on 22 December to 22:00 UTC on 23 December 2022, and (d–f) Cyclone Jasper, from 22:00 UTC on 12 December to 22:00 UTC on 13 December 2023. The three configurations are IDW-K5 (a, d), using the five nearest gauges without a maximum search distance; IDW-K5-L (b, e), using up to five nearest gauges within a 200-km search radius; and IDW-K20-L (c, f), using up to 20 nearest gauges within the same search radius. IDW-K5 corresponds to the IDW configuration used in Fig. 10.



845 **Figure 13**. Gauge-based precipitation estimates obtained using locally fitted two-dimensional thin-plate spline (TPS) interpolation for two selected extreme precipitation events: (a, b) Cyclone Ellie, from 22:00 UTC on 22 December to 22:00 UTC on 23 December 2022, and (c, d) Cyclone Jasper, from 22:00 UTC on 12 December to 22:00 UTC on 13 December 2023. The two configurations are TPS-K20 (a, c), fitted locally using the 20 nearest gauges, and TPS-K50 (b, d), fitted locally using the 50 nearest gauges. These estimates provide additional gauge-based interpolation examples for comparison
850 with the IDW estimates in Figs. 10 and 12.

5.3 Limitations and future directions

One limitation of the current framework is the propagation of residual errors from input observations into the blended analysis. Residual errors that are not identified through quality control, particularly for gauge observations, or are not fully removed by bias correction, particularly for satellite and radar estimates, can propagate into the blended analysis. Although

the statistical interpolation weighting accounts for the intensity-dependent error characteristics of each source, an individual source generally does not receive complete weight, as this would require the error of the other sources to become overwhelmingly large in comparison. Consequently, residual biases in sources retaining non-zero weights can propagate into the final analysis.

For example, during Cyclone Jasper, underestimation in the satellite estimates contributed to underestimation in BR-SRG even when radar closely represented the observed accumulation (Fig. 14b). Conversely, during Cyclone Ellie, radar substantially underestimated the observed accumulation, while the satellite estimates were higher and partly compensated for the radar underestimation in the blended analysis (Fig. 14a). These contrasting cases demonstrate the value of retaining complementary information from multiple data sources, rather than simply increasing the contribution of a single source.

Together with the relative differences among S1, R1, BR-SG, and BR-SRG in the rainfall-intensity analysis (Fig. 7), these cases suggest that residual underestimation in the satellite estimates may contribute to the negative bias observed in BR-SRG, although the intensity-stratified bias is also affected by observation-based stratification. Further improvements should therefore focus on bias correction, particularly in better accounting for systematic biases across different rainfall intensities.

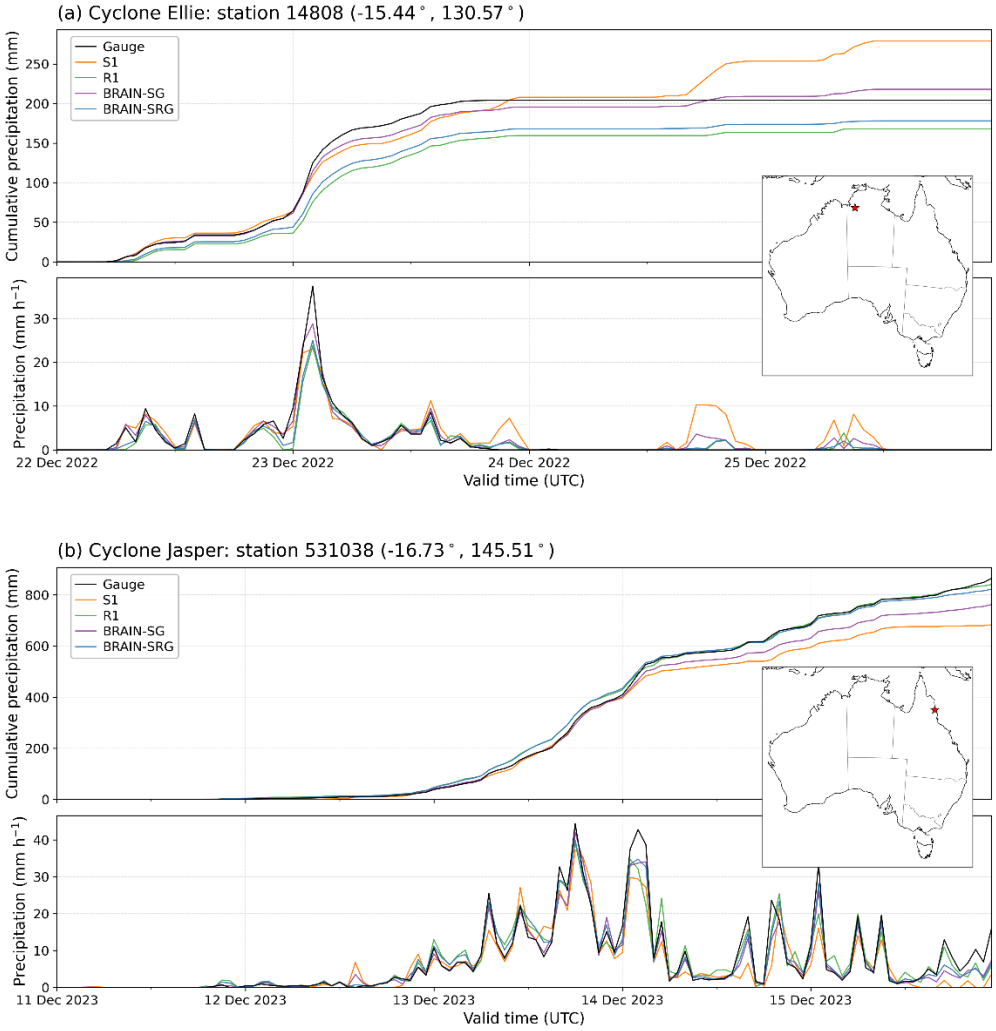


Figure 14. Temporal evolution of precipitation at selected gauge locations during (a) Cyclone Ellie and (b) Cyclone Jasper. Each panel shows cumulative precipitation (top) and hourly precipitation (bottom) from gauge observations and different rainfall estimates. Insets indicate the locations of the selected gauges.

A second limitation concerns the spatial continuity of the blended precipitation field, particularly across radar coverage boundaries. Outside radar coverage, the analysis is primarily constrained by the satellite background and gauge observations, whereas within radar coverage, radar observations provide an additional constraint and can strongly influence the analysis when their estimated errors are smaller. When satellite and radar estimates are broadly consistent, the transition is generally smooth. However, large discrepancies between the two sources can produce visible spatial transitions near radar coverage boundaries. This occurs because the analysis within radar coverage is adjusted towards radar when its estimated errors are much smaller than those of the satellite, while areas outside radar coverage remain primarily constrained by the satellite

background (Fig. 10). Importantly, radar information in the present framework is not restricted by a hard coverage boundary. Through error-informed localisation, surrounding radar observations can influence nearby areas beyond the nominal radar coverage, with their influence gradually decreasing with distance. This provides a smoother transition between radar-dominated and satellite-dominated regions than approaches relying solely on co-located observations, substantially reducing abrupt discontinuities at radar coverage boundaries. However, it cannot fully eliminate discontinuities when the input precipitation fields differ substantially. Improving consistency among input sources through better retrieval algorithm, quality control, and bias correction, together with incorporating additional independent data sources, could further improve spatial continuity.

A further consideration is the scale mismatch between point-based gauge observations and gridded precipitation estimates. Gauge measurements represent precipitation at individual locations, whereas satellite, radar, and blended estimates represent precipitation over grid cells. This representativeness difference affects not only the evaluation but also gauge-based bias correction and the estimation of error characteristics used in the blending framework. The effect can be particularly evident for localised and spatially variable hourly rainfall, where a point gauge may record substantially higher or lower rainfall than the corresponding grid-cell estimate (e.g., Fig. 10), particularly when local rainfall maxima occur within only a small fraction of the grid cell. Previous studies have attempted to quantify this uncertainty using dense gauge networks and point-to-area approaches (Bohnenstengel et al., 2011; Li et al., 2026; Tang et al., 2018), but it remains difficult to eliminate where gauge observations are sparse. Future work could explicitly characterise point-to-grid representativeness uncertainty as a function of gauge density, rainfall intensity, and spatial scale.

6 Conclusions

In this study, we developed and trialled BRAIN, a national-scale multi-source precipitation analysis system that blends Himawari satellite rainfall estimates, Rainfields radar products, and hourly gauge observations to generate a 2-km, hourly gridded rainfall analyses for Australia. The system addresses a long-standing need for high-resolution, sub-daily rainfall information by combining a unified statistical interpolation framework with computational strategies designed for continental-scale implementation. Comprehensive evaluation over a two-year trial period (2022–2023) demonstrates the overall benefit of integrating complementary satellite, radar, and gauge information. BR-SRG generally improved rainfall estimation compared with the individual input sources and simpler two-source configurations. The resulting analyses provide spatially complete and temporally continuous rainfall fields, supporting the potential application of the framework to both historical analysis and near-real-time rainfall estimation.

The key conclusions of this study can be summarised as follows:

(1) The high-frequency Himawari CRRPH product is demonstrated to be an effective background field for national-scale precipitation blending. Its key role is to provide a spatially complete first guess at very high spatial and

temporal resolution, onto which higher-accuracy radar and gauge observations can be integrated according to their estimated errors and spatial relationships. In regions where ground-based observations are sparse or absent, the satellite background effectively fills spatial gaps and maintains complete rainfall coverage across the continental domain. At the same time, the evaluation highlights the importance of bias correction and the remaining influence of satellite retrieval errors on the final analysis, particularly where ground-based observations are limited.

(2) The continental-scale trial demonstrates that all currently available and operationally manageable observation-based data sources in Australia, including satellite, radar, and gauge observations can be integrated within a unified statistical framework. The system is already under active testing within the Bureau's internal environment and is technically ready for operationalisation. In the longer term, the framework is designed to support both historical reconstruction and near-real-time product generation, providing a consistent and flexible rainfall analysis for a wide range of users.

(3) The error-informed localisation strategy embedded within the statistical interpolation framework is shown to be effective at continental scale. In particular, the nearest-point approximation for gridded radar substantially reduces modelling and computational complexity, enabling multi-source blending at kilometre and hourly resolutions over large spatial domains. The results demonstrate the practical feasibility of this approximation for large-scale implementation while retaining the major benefits of incorporating radar information.

(4) The added value of the blended product is confirmed through comprehensive comparisons. BR-SRG generally showed better overall performance than the individual satellite and radar estimates and the simpler two-source blending configurations. Gauge availability also affected the performance of gauge-dependent estimation processes, with greater improvements generally found under higher gauge-density conditions. Comparisons with the gauge-based IDW reference and daily operational AGCD product in selected cases further illustrate the benefit of incorporating spatially continuous satellite and radar information. The blended analysis captures finer-scale rainfall structures and spatial variations in rainfall intensity that are not fully represented by these products.

Future development of BRAIN will focus on improving input data quality, refining error characterisation, and enhancing spatial and temporal resolution. Error characterisation is performed offline using historical data. Therefore, introducing or updating an input product mainly requires repeating this offline estimation and subsequent evaluation, while the operational analysis remains computationally efficient. Anticipated upgrades to the Himawari-based CRRPH product are expected to further improve performance, particularly in tropical and radar-sparse regions, while ongoing radar recalibration efforts are likely to enhance local accuracy. The integration of complementary satellite products (e.g. IMERG), additional ground-based observations (including daily gauge observations and the expanding availability of third-party sub-daily gauge observations), and improved representation of error characteristics in sparsely observed regions will further strengthen the system (e.g., Zhang et al., 2027). Additional products, particularly satellite products, may also introduce cross-source error dependencies

due to shared retrieval methods and/or calibration procedures. The current independence assumption is a practical simplification and should therefore be re-evaluated when extending BRAIN to additional data sources.

Overall, BRAIN represents an important step towards an operational national sub-daily rainfall analysis capability for Australia. Beyond its immediate regional relevance, this study provides an additional reference for large-scale multi-source precipitation analysis systems at kilometre and hourly resolutions under heterogeneous observational conditions.

Data availability

The Himawari CRRPH satellite precipitation data can be accessed via the National Computational Infrastructure (NCI) Data Catalogue (https://dx.doi.org/10.25914/qc2q-mx21). Radar precipitation data are also available through the NCI Data Catalogue (https://dx.doi.org/10.25914/5cb686a8d9450). The BRAIN product is currently on pre-production test and working to allow its transition into production. Other datasets that are not openly accessible can be requested from the Australian Bureau of Meteorology.

Author contributions

YZ developed the methodology, performed the formal analysis, implemented the software, carried out the validation and visualization, and prepared the original draft of the manuscript. QW, AF, JP, BT, and CV contributed to the conceptualization, investigation, methodology, formal analysis, and validation of the study. AF, JP, BT, CV, and VV curated the datasets used in the analysis. QW, AF, and CV were responsible for funding acquisition, project administration, and supervision. AF and CV provided key resources supporting the study. CS contributed to the formal analysis, methodology, investigation, and validation. All authors contributed to manuscript review and editing and approved the final version.

Competing interests

The authors declare that they have no conflict of interest.

Disclaimer

Copernicus Publications remains neutral with regard to jurisdictional claims made in the text, published maps, institutional affiliations, or any other geographical representation in this paper. While Copernicus Publications makes every effort to include appropriate place names, the final responsibility lies with the authors. Views expressed in the text are those of the authors and do not necessarily reflect the views of the publisher.

Acknowledgements

We sincerely thank Bureau of Meteorology's scientists Dr. Zhi-Weng Chua, Dr. Caroline Poulsen for their valuable feedback during the internal review process of this manuscript. We also thank Dr. Mahadi Hasan for his assistance in processing the additional hourly gauge dataset and the Bureau's flood and data teams for support supplying that data. We gratefully acknowledge the numerous organisations and agencies across the Australian water sector for their contributions of flood and water information to the Bureau of Meteorology under the Water Act 2007. This research was undertaken with the assistance of resources and services provided by the National Computational Infrastructure (NCI Australia), which is supported by the Australian Government. This research has been funded by the Bureau of Meteorology as part of the Next Generation Rainfall Project.

References

Acharya, S. C., Nathan, R., Wang, Q. J., and Su, C.-H.: Temporal disaggregation of daily rainfall measurements using regional reanalysis for hydrological applications, Journal of Hydrology, 610, 127867, https://doi.org/10.1016/j.jhydrol.2022.127867, 2022.

Bari, M., Hasan, M., Evans, A., Frost, A., and Chua, Z.-W.: Development of operational 0.01-degree resolution gridded historical daily precipitation data for Australia, Journal of Southern Hemisphere Earth Systems Science, ES25008, https://doi.org/10.1071/ES25008, 2026.

Beck, H. E., van Dijk, A. I. J. M., Levizzani, V., Schellekens, J., Miralles, D. G., Martens, B., and de Roo, A.: MSWEP: 3-hourly 0.25deg, global gridded precipitation (1979-2015) by merging gauge, satellite, and reanalysis data, Hydrology and Earth System Sciences, 21, 589–615, https://doi.org/10.5194/hess-21-589-2017, 2017.

Beck, H. E., Wood, E. F., Pan, M., Fisher, C. K., Miralles, D. G., van Dijk, A. I. J. M., McVicar, T. R., and Adler, R. F.: MSWEP V2 Global 3-Hourly 0.1° Precipitation: Methodology and Quantitative Assessment, Bulletin of the American Meteorological Society, 100, 473–500, https://doi.org/10.1175/BAMS-D-17-0138.1, 2019.

Bergman, K. H.: Role of Observational Errors in Optimum Interpolation Analysis, Bulletin of the American Meteorological Society, 59, 1603–1611, https://doi.org/10.1175/1520-0477-59.12.1603, 1978.

Bhargava, M. and Danard, M.: Application of Optimum Interpolation to the Analysis of Precipitation in Complex Terrain, Journal of Applied Meteorology and Climatology, 33, 508–518, https://doi.org/10.1175/1520-0450(1994)033<0508:AOOITT>2.0.CO;2, 1994.

Bohnenstengel, S. I., Schlünzen, K. H., and Beyrich, F.: Representativity of in situ precipitation measurements – A case study for the LITFASS area in North-Eastern Germany, Journal of Hydrology, 400, 387–395, https://doi.org/10.1016/j.jhydrol.2011.01.052, 2011.

Bureau of Meteorology: AURA - Operational Radar Network Archive [data set], National Computational Infrastructure, https://dx.doi.org/10.25914/5cb686a8d9450, 2022.

Bureau of Meteorology: Himawari 8/9 - Convective Rain Rate - Physically Based (CRRPH) (V2.1) [data set], National Computational Infrastructure, https://dx.doi.org/10.25914/qc2q-mx21, 2024.

Bureau of Meteorology: Australia Rainfall and River Conditions, Bureau of Meteorology, Australian Government, http://www.bom.gov.au/australia/flood/ (last access: 20 February 2025), 2025.

Chappell, A., Renzullo, L. J., Raupach, T. H., and Haylock, M.: Evaluating geostatistical methods of blending satellite and gauge data to estimate near real-time daily rainfall for Australia, Journal of Hydrology, 493, 105–114, https://doi.org/10.1016/j.jhydrol.2013.04.024, 2013.

Chen, H., Wen, D., Du, Y., Xiong, L., and Wang, L.: Errors of five satellite precipitation products for different rainfall intensities, Atmospheric Research, 285, 106622, https://doi.org/10.1016/j.atmosres.2023.106622, 2023.

Chua, Z.-W., Kuleshov, Y., Watkins, A. B., Choy, S., and Sun, C.: A Two-Step Approach to Blending GSMaP Satellite Rainfall Estimates with Gauge Observations over Australia, Remote Sensing, 14, 1903, https://doi.org/10.3390/rs14081903, 2022a.

Chua, Z.-W., Evans, A., Kuleshov, Y., Watkins, A., Choy, S., and Sun, C.: Enhancing the Australian Gridded Climate Dataset rainfall analysis using satellite data, Scientific Report, 12, 20691, https://doi.org/10.1038/s41598-022-25255-6, 2022b.

Chua, Z.-W., Kuleshov, Y., Watkins, A. B., Choy, S., and Sun, C.: A Statistical Interpolation of Satellite Data with Rain Gauge Data over Papua New Guinea, Journal of Hydrometeorology, 24, 2369–2387, https://doi.org/10.1175/JHM-D-23-0035.1, 2023.

Chumchean, S., Seed, A., and Sharma, A.: Correcting of real-time radar rainfall bias using a Kalman filtering approach, Journal of Hydrology, 317, 123–137, https://doi.org/10.1016/j.jhydrol.2005.05.013, 2006.

Ciach, G. J.: Local Random Errors in Tipping-Bucket Rain Gauge Measurements, Journal of Atmospheric and Oceanic Technology, 20, 752–759, https://doi.org/10.1175/1520-0426(2003)20<752:LREITB>2.0.CO;2, 2003.

De Mey, P.: Optimal Interpolation in a model of the Azores Current in 1986–88, in: Data Assimilation: Tools for Modelling the Ocean in a Global Change Perspective, edited by: Brasseur, P. P. and Nihoul, J. C. J., Springer-Verlag, Berlin, Heidelberg, 85–105, https://doi.org/10.1007/978-3-642-78939-7_4, 1994.

Delrieu, G., Hucke, L., and Creutin, J. D.: Attenuation in Rain for X- and C-Band Weather Radar Systems: Sensitivity with respect to the Drop Size Distribution, Journal of Applied Meteorology and Climatology, 38, 57–68, https://doi.org/10.1175/1520-0450(1999)038<0057:AIRFXA>2.0.CO;2, 1999.

Dong, J., Crow, W. T., Chen, X., Tangdamrongsub, N., Gao, M., Sun, S., Qiu, J., Wei, L., Gao, H., and Duan, Z.: Statistical uncertainty analysis-based precipitation merging (SUPER): A new framework for improved global precipitation estimation, Remote Sensing of Environment, 283, 113299, https://doi.org/10.1016/j.rse.2022.113299, 2022.

Dunn, R. E., Fowler, H. J., Green, A. C., and Lewis, E.: Tipping-bucket rain gauges: a review of the undercatch phenomenon, and methods for its reduction and correction, Weather, 80, 196–205, https://doi.org/10.1002/wea.7736, 2025.

Evans, A., Jones, D., Smalley, R., and Lellyett, S.: An enhanced gridded rainfall analysis scheme for Australia, Bureau Research Report No. 041, Bureau of Meteorology, Melbourne, Australia, https://nla.gov.au/nla.obj-2786078795 (last access: 9 October 2026), 2020.

Fortin, V., Roy, G., Donaldson, N., and Mahidjiba, A.: Assimilation of radar quantitative precipitation estimations in the Canadian Precipitation Analysis (CaPA), Journal of Hydrology, 531, 296–307, https://doi.org/10.1016/j.jhydrol.2015.08.003, 2015.

Fortin, V., Roy, G., Stadnyk, T., Koenig, K., Gasset, N., and Mahidjiba, A.: Ten Years of Science Based on the Canadian Precipitation Analysis: A CaPA System Overview and Literature Review, Atmosphere-Ocean, 56, 178–196, https://doi.org/10.1080/07055900.2018.1474728, 2018.

Gandin, L. S.: Objective Analysis of Meteorological Fields, Israel Program for Scientific Translations, Jerusalem, 242 pp., 1965.

Gauthier, P., Tanguay, M., Laroche, S., Pellerin, S., and Morneau, J.: Extension of 3DVAR to 4DVAR: Implementation of 4DVAR at the Meteorological Service of Canada, Monthly Weather Review, 135, 2339–2354, https://doi.org/10.1175/MWR3394.1, 2007.

Gavahi, K., Foroumandi, E., and Moradkhani, H.: A deep learning-based framework for multi-source precipitation fusion, Remote Sensing of Environment, 295, 113723, https://doi.org/10.1016/j.rse.2023.113723, 2023.

Huang, X.-Y., Gustafsson, N., and Källén, E. R.: Using an adjoint model to improve an optimum interpolation-based data-assimilation system, Tellus A, 49, 161–176, https://doi.org/10.1034/j.1600-0870.1997.t01-1-00001.x, 1997.

Hubbert, J. C., Dixon, M., Ellis, S. M., and Meymaris, G.: Weather Radar Ground Clutter. Part I: Identification, Modeling, and Simulation, Journal of Atmospheric and Oceanic Technology, 26, 1165–1180, https://doi.org/10.1175/2009JTECHA1159.1, 2009a.

Hubbert, J. C., Dixon, M., and Ellis, S. M.: Weather Radar Ground Clutter. Part II: Real-Time Identification and Filtering, Journal of Atmospheric and Oceanic Technology, 26, 1181–1197, https://doi.org/10.1175/2009JTECHA1160.1, 2009b.

Hyfte, S. V., Moigne, P. L., Bazile, E., Verrelle, A., and Boone, A.: High-Resolution Reanalysis of Daily Precipitation using AROME Model Over France, Tellus A, 75, 27–49, https://doi.org/10.16993/tellusa.95, 2023.

Imhoff, R. O., De Cruz, L., Dewettinck, W., Brauer, C. C., Uijlenhoet, R., van Heeringen, K.-J., Velasco-Forero, C., Nerini, D., Van Ginderachter, M., and Weerts, A. H.: Scale-dependent blending of ensemble rainfall nowcasts and numerical weather prediction in the open-source pysteps library, Quarterly Journal of the Royal Meteorological Society, 149, 1335–1364, https://doi.org/10.1002/qj.4461, 2023.

Islam, Md. A., Yu, B., and Cartwright, N.: Assessment and comparison of five satellite precipitation products in Australia, Journal of Hydrology, 590, 125474, https://doi.org/10.1016/j.jhydrol.2020.125474, 2020.

Jeffrey, S. J., Carter, J. O., Moodie, K. B., and Beswick, A. R.: Using spatial interpolation to construct a comprehensive archive of Australian climate data, Environmental Modelling & Software, 16, 309–330, https://doi.org/10.1016/S1364-8152(01)00008-1, 2001.

Jones, D., Wang, W., and Fawcett, R.: High-quality spatial climate data-sets for Australia, Australian Meteorological and Oceanographic Journal, 58, 233–248, https://doi.org/10.22499/2.5804.003, 2009.

Karagiannidis, A., Lahuerta, J. A., Calbet, X., Lliso, L., Lagouvardos, K., Kotroni, V., and Ripodas, P.: Efficiency of the NWC SAF Version 2021 CRRPh Precipitation Product: Comparison against Previous NWC SAF Precipitation Products and the Influence of Topography, Climate, 11, 34, https://doi.org/10.3390/cli11020034, 2023.

Khedhaouiria, D., Bélair, S., Fortin, V., Roy, G., and Lespinas, F.: High-Resolution (2.5 km) Ensemble Precipitation Analysis across Canada, Journal of Hydrometeorology, 21, 2023–2039, https://doi.org/10.1175/JHM-D-19-0282.1, 2020.

Khedhaouiria, D., Bélair, S., Fortin, V., Roy, G., and Lespinas, F.: Using a hybrid optimal interpolation–ensemble Kalman filter for the Canadian Precipitation Analysis, Nonlinear Processes in Geophysics, 29, 329–344, https://doi.org/10.5194/npg-29-329-2022, 2022.

Kirsch, B., Clemens, M., and Ament, F.: Stratiform and Convective Radar Reflectivity–Rain Rate Relationships and Their Potential to Improve Radar Rainfall Estimates, Journal of Applied Meteorology and Climatology, 58, 2259–2271, https://doi.org/10.1175/JAMC-D-19-0077.1, 2019.

Kossieris, P., Tsoukalas, I., Brocca, L., Mosaffa, H., Makropoulos, C., and Anghelea, A.: Precipitation data merging via machine learning: Revisiting conceptual and technical aspects, Journal of Hydrology, 637, 131424, https://doi.org/10.1016/j.jhydrol.2024.131424, 2024.

Koster, R. D., Liu, Q., Reichle, R. H., and Huffman, G. J.: Improved Estimates of Pentad Precipitation Through the Merging of Independent Precipitation Data Sets, Water Resources Research, 57, e2021WR030330, https://doi.org/10.1029/2021WR030330, 2021.

Li, Y., Han, B., Chen, L., Zhou, R., and Li, R.: Refine the Uncertainty of GPM IMERG Precipitation Product Accounting for the Inherent Error From Rain Gauges Estimations, Earth and Space Science, 13, e2025EA004745, https://doi.org/10.1029/2025EA004745, 2026.

Lorenc, A. C., Bell, R. S., and Macpherson, B.: The Meteorological Office analysis correction data assimilation scheme, Quarterly Journal of the Royal Meteorological Society, 117, 59–89, https://doi.org/10.1002/qj.49711749704, 1991.

Ma, Z., Xu, J., Dong, B., Hu, X., Hu, H., Yan, S., Zhu, S., He, K., Shi, Z., Chen, Y., Fang, X., Zhang, Q., Gu, S., and Weng, F.: GMCP: A Fully Global Multisource Merging-and-Calibration Precipitation Dataset (1-Hourly, 0.1°, Global, 2000–the Present), Bulletin of the American Meteorological Society, 106, E596–E624, https://doi.org/10.1175/BAMS-D-24-0051.1, 2025.

Mahfouf, J., Brasnett, B., and Gagnon, S.: A Canadian precipitation analysis (CaPA) project: Description and preliminary results, Atmosphere-Ocean, 45, 1–17, https://doi.org/10.3137/ao.v450101, 2007.

Malone, T.: Using URBS for Real Time Flood Modelling, in: Water 99 Joint Congress: 25th Hydrology & Water Resources Symposium and 2nd International Conference on Water Resources & Environment Research, Brisbane, Australia, 6–8 July 1999, Institution of Engineers, Australia, Barton, ACT, 603–608, https://doi.org/10.3316/informit.ENG_70A, 1999.

Malone, T. and Carroll, D.: Guidelines for URBS routing parameters, in: 40th Hydrology & Water Resources Symposium 2022 (HWRS 2022): The Past, the Present, the Future, Brisbane, Australia, 30 November–2 December 2022, Engineers Australia, https://microsites.arinex.com.au/HWRS/pdf/full-paper_19.pdf, 2022.

Martinaitis, S. M., Osborne, A. P., Simpson, M. J., Zhang, J., Howard, K. W., Cocks, S. B., Arthur, A., Langston, C., and Kaney, B. T.: A Physically Based Multisensor Quantitative Precipitation Estimation Approach for Gap-Filling Radar Coverage, Journal of Hydrometeorology, 21, 1485–1511, https://doi.org/10.1175/JHM-D-19-0264.1, 2020.

McRoberts, D. B. and Nielsen-Gammon, J. W.: Detecting Beam Blockage in Radar-Based Precipitation Estimates, Journal of Atmospheric and Oceanic Technology, 34, 1407–1422, https://doi.org/10.1175/JTECH-D-16-0174.1, 2017.

Mitchell, H. L., Charette, C., Chouinard, C., and Brasnett, B.: Revised Interpolation Statistics for the Canadian Data Assimilation Procedure: Their Derivation and Application, Monthly Weather Review, 118, 1591–1614, https://doi.org/10.1175/1520-0493(1990)118<1591:RISFTC>2.0.CO;2, 1990.

Nguyen, C., Vaze, J., Mateo, C. M. R., Hutchinson, M. F., and Teng, J.: Elevation dependent spatial interpolation of hourly rainfall for accurate flood inundation modelling, Hydrology and Earth System Sciences, 30, 45–66, https://doi.org/10.5194/hess-30-45-2026, 2026.

Nishant, N., Sherwood, S., Prasad, A., Ji, F., and Singh, A.: Impact of Higher Spatial Resolution on Precipitation Properties Over Australia, Geophysical Research Letters, 49, e2022GL100717, https://doi.org/10.1029/2022GL100717, 2022.

Ochoa-Rodriguez, S., Wang, L.-P., Willems, P., and Onof, C.: A Review of Radar-Rain Gauge Data Merging Methods and Their Potential for Urban Hydrological Applications, Water Resources Research, 55, 6356–6391, https://doi.org/10.1029/2018WR023332, 2019.

Prein, A. F., Rasmussen, R. M., Ikeda, K., Liu, C., Clark, M. P., and Holland, G. J.: The future intensification of hourly precipitation extremes, Nature Climate Change, 7, 48–52, https://doi.org/10.1038/nclimate3168, 2017.

Rabier, F.: Overview of global data assimilation developments in numerical weather-prediction centres, Quarterly Journal of the Royal Meteorological Society, 131, 3215–3233, https://doi.org/10.1256/qj.05.129, 2005.

Rabier, F., Järvinen, H., Klinker, E., Mahfouf, J.-F., and Simmons, A.: The ECMWF operational implementation of four-dimensional variational assimilation. I: Experimental results with simplified physics, Quarterly Journal of the Royal Meteorological Society, 126, 1143–1170, https://doi.org/10.1002/qj.49712656415, 2000.

Rawlins, F., Ballard, S. P., Bovis, K. J., Clayton, A. M., Li, D., Inverarity, G. W., Lorenc, A. C., and Payne, T. J.: The Met Office global four-dimensional variational data assimilation scheme, Quarterly Journal of the Royal Meteorological Society, 133, 347–362, https://doi.org/10.1002/qj.32, 2007.

Renzullo, L. J., Velasco-Forero, C. A., and Seed, A. W.: Blending radar, NWP and satellite data for real-time ensemble rainfall analysis: a scale-dependent method, CSIRO, Technical Report EP174236, https://doi.org/10.4225/08/594eb78c96025, 2017.

Seed, A., Duthie, E., and Chumchean, S.: Rainfields: the Australian Bureau of Meteorology system for quantitative precipitation estimation, in: Proceedings 33rd AMS Conference on Radar Meteorology, Cairns, Australia, 6–10 August 2007, American Meteorological Society, https://ams.confex.com/ams/33Radar/techprogram/paper_123340.htm, 2007.

Segovia-Cardozo, D. A., Bernal-Basurco, C., and Rodríguez-Sinobas, L.: Tipping Bucket Rain Gauges in Hydrological Research: Summary on Measurement Uncertainties, Calibration, and Error Reduction Strategies, Sensors, 23, 5385, https://doi.org/10.3390/s23125385, 2023.

Seo, B.-C. and Krajewski, W. F.: Investigation of the scale-dependent variability of radar-rainfall and rain gauge error covariance, Advances in Water Resources, 34, 152–163, https://doi.org/10.1016/j.advwatres.2010.10.006, 2011.

Shen, Y., Zhao, P., Pan, Y., and Yu, J.: A high spatiotemporal gauge-satellite merged precipitation analysis over China, Journal of Geophysical Research: Atmospheres, 119, 3063–3075, https://doi.org/10.1002/2013JD020686, 2014.

Shen, Y., Hong, Z., Pan, Y., Yu, J., and Maguire, L.: China's 1 km Merged Gauge, Radar and Satellite Experimental Precipitation Dataset, Remote Sensing, 10, 264, https://doi.org/10.3390/rs10020264, 2018.

So, D. and Shin, D.-B.: Classification of precipitating clouds using satellite infrared observations and its implications for rainfall estimation, Quarterly Journal of the Royal Meteorological Society, 144, 133–144, https://doi.org/10.1002/qj.3288, 2018.

Su, C.-H., Eizenberg, N., Steinle, P., Jakob, D., Fox-Hughes, P., White, C. J., Rennie, S., Franklin, C., Dharssi, I., and Zhu, H.: BARRA v1.0: the Bureau of Meteorology Atmospheric high-resolution Regional Reanalysis for Australia, Geoscientific Model Development, 12, 2049–2068, https://doi.org/10.5194/gmd-12-2049-2019, 2019.

Su, C.-H., Eizenberg, N., Jakob, D., Fox-Hughes, P., Steinle, P., White, C. J., and Franklin, C.: BARRA v1.0: kilometre-scale downscaling of an Australian regional atmospheric reanalysis over four midlatitude domains, Geoscientific Model Development, 14, 4357–4378, https://doi.org/10.5194/gmd-14-4357-2021, 2021.

Su, C.-H., Torrance, J., Rennie, S., Howard, E., Stassen, C., Warren, R., Smith, A., Dharssi, I., Pepler, A., Tian, S., Lipson, M., Steinle, P., Franklin, C., Le, T., Wang, C., Masoumi, S., and Le Marshall, J.: The Australian regional atmospheric reanalysis system, version 2 – BARRA2, Journal of Southern Hemisphere Earth Systems Science, 75, ES25032, https://doi.org/10.1071/ES25032, 2025.

Sun, Q., Miao, C., Duan, Q., Ashouri, H., Sorooshian, S., and Hsu, K.: A Review of Global Precipitation Data Sets: Data Sources, Estimation, and Intercomparisons, Reviews of Geophysics, 56, 79–107, https://doi.org/10.1002/2017RG000574, 2018.

Tang, G., Behrangi, A., Long, D., Li, C., and Hong, Y.: Accounting for spatiotemporal errors of gauges: A critical step to evaluate gridded precipitation products, Journal of Hydrology, 559, 294–306, https://doi.org/10.1016/j.jhydrol.2018.02.057, 2018.

Upadhyaya, S. A., Kirstetter, P.-E., Gourley, J. J., and Kuligowski, R. J.: On the Propagation of Satellite Precipitation Estimation Errors: From Passive Microwave to Infrared Estimates, Journal of Hydrometeorology, 21, 1367–1381, https://doi.org/10.1175/JHM-D-19-0293.1, 2020.

Villarini, G., Mandapaka, P. V., Krajewski, W. F., and Moore, R. J.: Rainfall and sampling uncertainties: A rain gauge perspective, Journal of Geophysical Research: Atmospheres, 113, D11102, https://doi.org/10.1029/2007JD009214, 2008.

Xia, H. and Wang, K.: Hourly, kilometer-scale precipitation merged from rain gauge, ground-based radar and satellites over east Asia: methods, evaluation and applications, Journal of Hydrology, 662, 134148, https://doi.org/10.1016/j.jhydrol.2025.134148, 2025.

Xie, P. and Xiong, A.-Y.: A conceptual model for constructing high-resolution gauge-satellite merged precipitation analyses, Journal of Geophysical Research: Atmospheres, 116, D21106, https://doi.org/10.1029/2011JD016118, 2011.

Xie, P., Chen, M., and Shi, W.: CPC unified gauge-based analysis of global daily precipitation, in: 24th Conference on Hydrology, Atlanta, GA, USA, 18 January 2010, American Meteorological Society, presentation 2.3A, https://ams.confex.com/ams/90annual/webprogram/Paper163676.html, 2010.

Xu, L., Chen, N., Moradkhani, H., Zhang, X., and Hu, C.: Improving Global Monthly and Daily Precipitation Estimation by Fusing Gauge Observations, Remote Sensing, and Reanalysis Data Sets, Water Resources Research, 56, e2019WR026444, https://doi.org/10.1029/2019WR026444, 2020.

Xu, Y., Tang, G., Li, L., and Wan, W.: Multi-source precipitation estimation using machine learning: Clarification and benchmarking, Journal of Hydrology, 635, 131195, https://doi.org/10.1016/j.jhydrol.2024.131195, 2024.

Yin, J., Guo, S., Gu, L., Zeng, Z., Liu, D., Chen, J., Shen, Y., and Xu, C.-Y.: Blending multi-satellite, atmospheric reanalysis and gauge precipitation products to facilitate hydrological modelling, Journal of Hydrology, 593, 125878, https://doi.org/10.1016/j.jhydrol.2020.125878, 2021.

Yu, J., Li, X.-F., Lewis, E., Blenkinsop, S., and Fowler, H. J.: UKGrsHP: a UK high-resolution gauge–radar–satellite merged hourly precipitation analysis dataset, Climate Dynamics, 54, 2919–2940, https://doi.org/10.1007/s00382-020-05144-2, 2020.

Zhang, W., Furtado, K., Wu, P., Zhou, T., Chadwick, R., Marzin, C., Rostron, J., and Sexton, D.: Increasing precipitation variability on daily-to-multiyear time scales in a warmer world, Science Advances, 7, eabf8021, https://doi.org/10.1126/sciadv.abf8021, 2021a.

Zhang, Y., Ye, A., Nguyen, P., Analui, B., Sorooshian, S., and Hsu, K.: Error Characteristics and Scale Dependence of Current Satellite Precipitation Estimates Products in Hydrological Modeling, Remote Sensing, 13, 3061, https://doi.org/10.3390/rs13163061, 2021b.

Zhang, Y., Ye, A., Nguyen, P., Analui, B., Sorooshian, S., and Hsu, K.: New Insights Into Error Decomposition for Precipitation Products, Geophysical Research Letters, 48, e2021GL094092, https://doi.org/10.1029/2021GL094092, 2021c.

Zhang, Y., Wang, Q. J., Frost, A. J., Trewin, B., Pudashine, J., Velasco-Forero, C., Su, C.-H., and Villani, V.: Advancing High-Resolution Precipitation Analysis for Operational Hydrological Applications in Australia: Data Sources, Methodologies, and Recommendations, WIREs Water, 12, e70037, https://doi.org/10.1002/wat2.70037, 2025.

Zhang, Y., Wang, Q. J., Frost, A. J., Pudashine, J., Trewin, B., Velasco-Forero, C., Su, C.-H., and Villani, V.: A localisation strategy for scalable and efficient multi-source precipitation blending at high resolutions over large domains, Journal of Hydrology, 677, 135831, https://doi.org/10.1016/j.jhydrol.2026.135831, 2026.

Zhang, Y., Wang, Q. J., Frost, A. J., Pudashine, J., Trewin, B., Velasco-Forero, C., Su, C.-H., Hasan, M. M., and Villani, V.: When radar and hourly gauges are scarce: Sharpening gridded precipitation estimates using daily observations, Atmospheric Research, 345, 109368, https://doi.org/10.1016/j.atmosres.2026.109368, 2027.

Zhu, S., Tang, G., Sorooshian, S., Huffman, G. J., Duan, Q., Yan, S., Behrangi, A., Papalexiou, S. M., Nguyen, P., Hsu, K., Wen, Y., Liu, Z., Li, Z., Chen, M., Laviola, S., and Hong, Y.: A Review of the Past Half Century of Geostationary Satellite Thermal Observations for Global Precipitation Estimation: Developments, achievements, and future prospects, IEEE Geoscience and Remote Sensing Magazine, 14, 369–391, https://doi.org/10.1109/MGRS.2026.3665828, 2026.